Progress in Quantum Electronics 98 (2024) 100537

Contents lists available at ScienceDirect

Progress in Quantum Electronics

journal homepage: www.elsevier.com/locate/pqe

Elemental segregation and dimensional separation in halide perovskite light-emitting diodes

Seok Joo Yang [a,b,1], Yoon Ho Lee [a,c,d,1], Kagachi Tateno [a], Letian Dou [a,c,e,*,2]

[a] Davidson School of Chemical Engineering, Purdue University, West Lafayette, IN, 47907, United States
[b] Department of Chemical Engineering, Kumoh National Institute of Technology, Gumi, 39177, Republic of Korea
[c] Department of Chemistry, Purdue University, West Lafayette, IN, 47907, United States
[d] Department of Environment and Energy Engineering, Sungshin Women's University, Seoul, 01133, Republic of Korea
[e] Birck Nanotechnology Center, Purdue University, West Lafayette, IN, 47907, United States

ARTICLE INFO

Keywords:
Cation segregation
Sn oxidation
Halide segregation
N phase separation
Perovskite LED

ABSTRACT

Compositional engineering is a promising avenue for enhancing external quantum efficiency and adjusting emission wavelengths in halide perovskite light-emitting diodes (PeLEDs). However, the occurrence of ion migration within these materials poses a notable challenge as it can lead to elemental segregation during crystallization or under external stimuli such as heat, light, and bias, especially when simple mixing and alloying are employed. Such non-uniform distribution of elements detrimentally impacts color purity and long-term device stability in PeLEDs, highlighting the need to address elemental segregation issues. Additionally, quasi-2D perovskites have garnered attention for their potential to mitigate ion migration while maintaining superior optoelectronic properties attributable to the quantum confinement effect. Nevertheless, precise control over dimensionality remains challenging due to the thermodynamically favored 2D/3D phase separation, hindering efficient energy transfer. This review aims to provide an in-depth analysis of these phenomena. It explores the underlying mechanisms of elemental segregation and dimensionality separation, while summarizing recent efforts to overcome these challenges. Furthermore, the review discusses ongoing obstacles and suggests potential directions for future research in this evolving field.

1. Introduction

The halide perovskite light-emitting diode (PeLED) has been emerging as a promising solid-state lighting technology because of its advantages of low-cost solution applicability, narrow electroluminescence (EL) spectra with full-width at half-maximum (FWHM) of around 20 nm, and tunable EL emission wavelengths [1–3]. The halide perovskites having ABX_3 formula, where A is a monovalent cation, which can be either an organic cation (e.g., methylammonium$^+$ and formamidinium$^+$) or an inorganic cation (e.g., Cs^+ and Rb^+), B is a divalent metal cation, and X is a halide anion, have been developed by compositional engineering to enhance optoelectronic properties of the halide perovskite films, which contributes to evolution of PeLED devices to have an external quantum efficiency (EQE) of over 30 % and half-lifetime of 30,000 h for operational stability (estimated, at 100 cd m^{-2}) [4–6]. Bandgaps of the

* Corresponding author. Davidson School of Chemical Engineering, Purdue University, West Lafayette, IN, 47907, United States.
E-mail address: dou10@purdue.edu (L. Dou).
[1] These authors contributed equally.
[2] Lead contact.

https://doi.org/10.1016/j.pquantelec.2024.100537
Received 28 March 2024; Received in revised form 11 October 2024; Accepted 6 November 2024
Available online 8 November 2024

halide perovskites are highly dependent on the compositions of A, B, and X, which are determined by hybridization of metal halide orbitals [7]. The conduction band minimum (CBM) is identified as anti-bonding states of the *p* orbital of the B-site metal and the *s* orbital of the X-site halogen, and the valence band maximum (VBM) corresponds to anti-bonding states of the *s* orbital of the B-site metal and the *p* orbital of the X-site halogen [7]. Thus, mixing halide ions can have a great impact on the bandgap tuning. In $CsPbX_3$ perovskites, slight CBM upshift from Pb – X distance and VBM downshift from strong electronegativity from I to Br and Cl enlarge the perovskite bandgaps (Fig. 1a). Based on low electronegativity of Sn compared to Pb, atomic levels of an Sn atom shift to upper direction, and a large upshift of VBM induces narrower bandgap in Sn perovskites (Fig. 1b). A-site cations affect lattice volume and distortion, slightly tuning the bandgap. For instance, when Cs^+ is replaced by methylammonium (MA^+) and formamidinium (FA^+), the bandgap is enlarged in $ASnCl_3$ perovskites (Fig. 1c), while the bandgap of $APbI_3$ perovskites is narrowed [8]. According to various elemental combinations, perovskites can emit various color ranges from violet to near-infrared (NIR), depicted in Fig. 1d [1,9]. In addition, mixing elements increases structural phase stability of perovskite crystals [10]. A-site cations geometrically occupy the central position of the perovskite framework, determining the dimensionality and directly influencing the stability, especially for phase stability [11,12]. The tolerance factor (*t*) is one of the indices to measure the phase stability and distortion of the perovskite crystal structure [13]. The following equation shows the *t* of ABX_3 perovskites,

$$t = \frac{r_A + r_X}{\sqrt{2}(r_B + r_X)}$$

where r_A, r_B, and r_x are the ionic radius of the A-, B-, and X-site ions, respectively. Generally, a perovskite structure with high power generation capacity is stably formed when the *t* value is between 0.8 and 1.0 (Fig. 1e) [10]. In the case of $MAPbI_3$, where the *t* value is 0.9, the perovskite structure is geometrically stable. On the other hand, for $FAPbI_3$ with a large radius of the A-site cation, the *t* value is out of the range, which makes the perovskite structure easy to form a photo-inactive phase. A small amount of alkali metal ions such as Cs and Rb can be partially replaced with the A-site to control the crystal structure and to improve the structural, moisture, and thermal stabilities [14–16]. Based on the diverse advantages, mixing elements in perovskite crystals is a widely used strategy for PeLED devices.

However, elemental segregation originating from ion migration hinders these optoelectronic characteristics. Unbalanced local elemental variations act as defects and further lead to degradation of perovskite crystals [17]. In addition, the ion migration can shift the recombination zone and EL spectra in PeLEDs according to local elemental-rich and -deficient domains [18]. For instance, halide segregation into I-rich and Br-rich regions in I-Br mixed halide perovskites has non-uniform properties from I-rich or Br-rich regions. Energy transfer from Br-rich region (larger bandgap) to I-rich region (narrower bandgap) induces redshifted EL emission in PeLEDs [19]. Therefore, suppressing ion migration is the most important factor for long lifetime, wavelength selectivity, and high color purity of PeLEDs [20]. Ion migration depending on different types of elements has been calculated with various assumptions such as ion migration pathways [21], types of Schottky and Frenkel defects [21–23], and lattice distortion [23]. The absolute values of activation energy for ion migration (E_a) are different depending on the assumptions. However, the tendency of E_a in $MAPbI_3$ is identical as $I^- < MA^+ \ll Pb^{2+}$ in order. Based on the calculation of E_a, halide ions most readily migrate under electric bias, and A-site cations migrate to

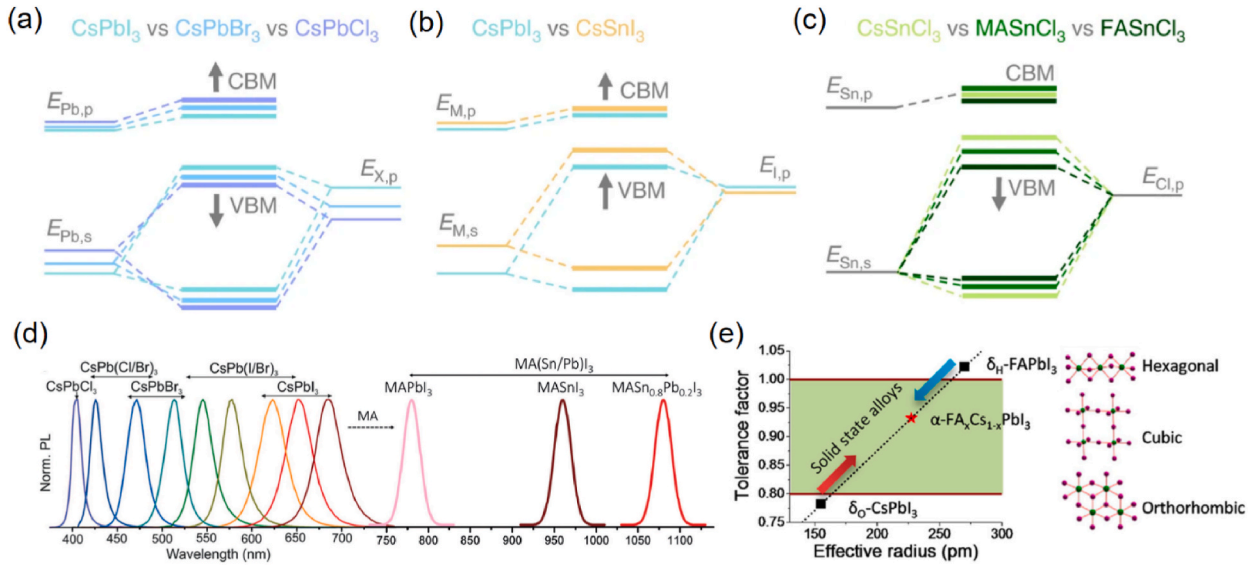

Fig. 1. Schematic energy levels of (a) $CsPbX_3$ perovskites (X = I, Br, and Cl), (b) $CsBI_3$ perovskites (B = Pb and Sn) and (c) $ASnCl_3$ perovskites (A = Cs, MA, and FA) [7]. Copyright 2019 Springer Nature. (d) PL spectra of the colloidal mixed-halide perovskite of $CsPbX_3$ and mixed metal-cation perovskite of $MA(Sn/Pb)I_3$ [1,9]. Copyright 2015 American Chemical Society and Copyright 2016 Wiley. (e) Crystal structures of halide perovskites based on Goldschmidt tolerance factor [10]. Copyright 2016 American Chemical Society.

the opposite direction of the halide ion migration, while ion migration of B-site cations is negligible. Thereby, elemental segregation has been widely studied by suppressing ion migration of A-site cations and halide ions in optoelectronics.

Two-dimensional (2D) perovskites have been vigorously studied due to their superior chemical stability compared to three-dimensional (3D) perovskites, and their unique optoelectronic properties come from the quantum confinement effect [24,25]. When a bulky organic cation is introduced into the A-site in ABX_3 perovskites, the bulky organic cation enters between the metal halide octahedrons, reducing the dimensionality from 3D to 2D. The thickness of the metal halide octahedron, which is n number, represents the degree of quantum confinement. Quasi-2D perovskites indicate multiple layers of the metal halide octahedron layers, not the single layer of complete 2D perovskites ($n = 1$). Quantum confinement occurs due to the potential barrier between the bulky organic cation and metal halide octahedron, leading to a large bandgap and high exciton binding energy (a few hundred meV) [26,27]. Therefore, the emission wavelength can be adjusted through bandgap tuning by controlling n numbers, and low dimensionality increases radiative recombination with high exciton binding energy, resulting in quasi-2D perovskites being in the spotlight in PeLED research fields. However, the quasi-2D perovskite is easily separated into 2D and 3D phases. This makes it difficult to obtain excellent optoelectronic properties from fine control of n numbers according to quantum confinement.

In this review, we differentiate between elemental segregation in 3D perovskites and phase segregation in quasi-2D perovskites. Section 2 is dedicated to 3D perovskites with the ABX_3 structure, where elemental segregation at the A, B, and X sites is explored in detail (as depicted in Fig. 2). In contrast, Section 3 addresses quasi-2D perovskites, with a focus on those adopting the A'_2BX_4 Ruddlesden-Popper 2D structure (A' is a bulky cation). Here, the phase separation refers to the structural segregation between the A'_2BX_4 and ABX_3 phases, which is a more complex process than the elemental segregation of A and A' cations. Given the distinct nature of the phase separation, it is discussed independently to provide a more comprehensive understanding of the differences between 3D and quasi-2D perovskites. Finally, in section 4, we offer a concise conclusion and outlook for future research directions. While previous review articles have extensively investigated elemental segregation in 3D perovskites and phase separation in quasi-2D perovskites individually, there is a lack of research on their similarities, differences, and a potential interplay between them. Here, we provide a comprehensive analysis of both phenomena, addressing their combined impact on PeLEDs, mainly discussed in Section 3.2. By exploring how elemental segregation and phase separation originate from and influence each other, we offer deeper insights into their effects on the optoelectronic properties and device performance of PeLEDs.

2. Elemental segregation in 3D perovskites

2.1. A-site cation segregation

2.1.1. A-site cation segregation from crystallization

A strategy of mixing cations is one of the efficient ways to enhance both device performance and operational stability of PeLEDs [28–32]. The single A-site cation based perovskites show obvious advantages and disadvantages. $MAPbI_3$ is thermodynamically unstable due to the hygroscopic and volatile properties of the MA cation, but it has a high structural phase stability. In contrast, $FAPbI_3$ shows higher thermal stability, but the photoactive black phase (α-$FAPbI_3$) is spontaneously degraded into the yellow phase (δ-$FAPbI_3$) under ambient conditions [33]. On the other hand, the double A-site cation based perovskites that include a mixture of MA and FA have been proven to have great potential to stabilize the crystal lattice [34]. In this regard, Grätzel et al. achieved a pure black phase of FA-MA perovskite systems via a sequential deposition method [35]. The longer exciton lifetime in $MA_{0.6}FA_{0.4}PbI_3$ can be attributed to superior carrier-collection efficiency compared to $MAPbI_3$, and the formation of δ-$FAPbI_3$ is suppressed in $MA_{0.6}FA_{0.4}PbI_3$. However, recent studies have demonstrated that the mixed cation perovskites suffer from cation segregation issues. Emsley et al. characterized

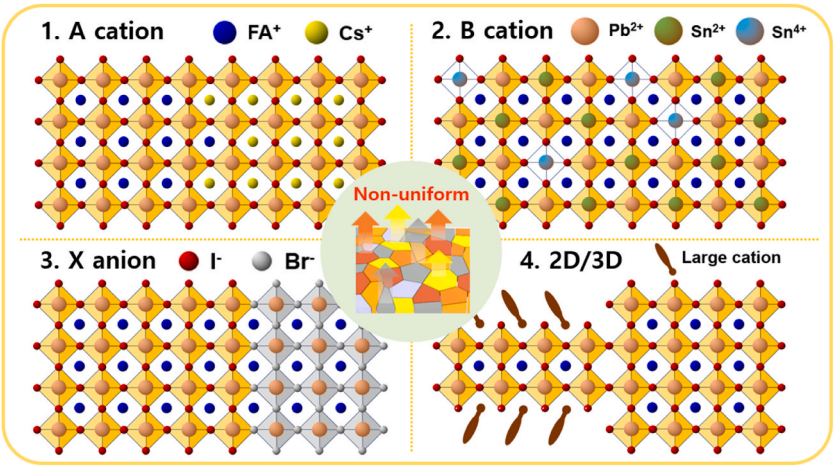

Fig. 2. Schematic illustration of heterogeneous perovskite films which is categorized into elemental (A, B, and X) segregation and dimensional separation.

the segregation of Cs in FA-Cs mixed cation perovskite films using Cs solid-state nuclear magnetic resonance (NMR) spectra analysis to deliver quantitative information of all the species for a given nucleus in the samples, regardless of the crystallinity [36]. When Cs contents are lower than 15 mol%, Cs is readily incorporated into the FA-based perovskite lattice. However, when the Cs contents are greater than 15 mol %, the second δ-$CsPbI_3$ phase is observed (Fig. 3a). The chemical shift simulation for the Cs is calculated using density-functional theory (DFT) for both a cubic and a tetragonal $FAPbI_3$ perovskite lattice where FA is replaced by Cs. The corresponding theoretical Cs shift of the lattice distortion from cubic to tetragonal is well-matched with what is observed in the experimental results. On the similar FA-Cs system, Pan et al. visualized the spatially inhomogeneous Cs and FA distribution along the vertical direction across perovskite films employing the grazing incident X-ray diffraction (GIXRD) technique to detect the crystal structure of the bottom interface by peeling off the sample from the bottom substrate (Fig. 3b) [37]. 1-(phenylsulfonyl) pyrrole (PSP) was employed as an additive to inhibit the A-site cation segregation in FA-Cs perovskites. In the reference (Ref.) sample, GIXRD shoulder peaks are emerged at about 28.4° when the grazing incidence angle is lower than 2.0° (Fig. 3c). In contrast, the shoulder peaks become negligibly small when the PSP is introduced in the FA-Cs perovskites (Fig. 3d). The shoulder peaks can be attributed to a Cs-rich phase caused by Cs incorporation following the coherence between 2θ and the lattice space [38,39]. The Cs-rich phase prefers to be located at the bottom of the perovskite film, thus leading to a gradient in the phase distribution from Cs-rich to Cs-poor from the bottom surface to the top, resulting in a spatially out-of-plane lattice mismatch in FA-Cs perovskite films due to the size difference of FA and Cs cations. In addition to A-site segregation of the FA-Cs based perovskite system, Kuno et al. conducted spatially resolved infrared (IR) measurements to determine cation-specific local inhomogeneity within FA-MA based perovskite films [40]. IR spectroscopy was performed as a function of cation stoichiometry to deliver spatial information in cation distributions for the FA-MA based perovskites [41]. The IR imaging using an infrared photothermal heterodyne imaging (IR-PHI) map shows that FA and MA are not alloyed uniformly but segregated into MA or FA-rich regions (Fig. 3e). The average MA/FA variations are around 20 %, three times higher than expected. The local cation inhomogeneity is caused by the differences in the kinetics of local $MAPbI_3$ and $FAPbI_3$ lattice formation. The $MAPbI_3$ and $FAPbI_3$ have tetragonal and cubic crystal structures, respectively, which are expected to be stabilized in the local environment with different compositions.

2.1.2. A-site cation segregation under external stress conditions

In addition to the cation segregation triggered by crystallization, aging conditions can also drive the segregation phenomena. Huang et al. demonstrated that excess carriers reduced E_a [42]. $FA_{0.7}Cs_{0.3}PbI_3$ perovskite film was utilized to examine the influence of excess charge carriers on cation migration. Polystyrene (PS), poly [bis(4-phenyl) (2,4,6-trimethylphenyl) amine] (PTAA) and phenyl-C 61-butyric acid methyl ester (PCBM) were applied on the perovskite films to induce non-quenching of charge carriers, excess electrons and holes, respectively. Blue shifts of photoluminescence (PL) spectra are observed under illumination from all the films, which is probably attributed to the formation of the Cs-rich phase. Notably, the perovskite film covered by PCBM had the most rapid shift in PL

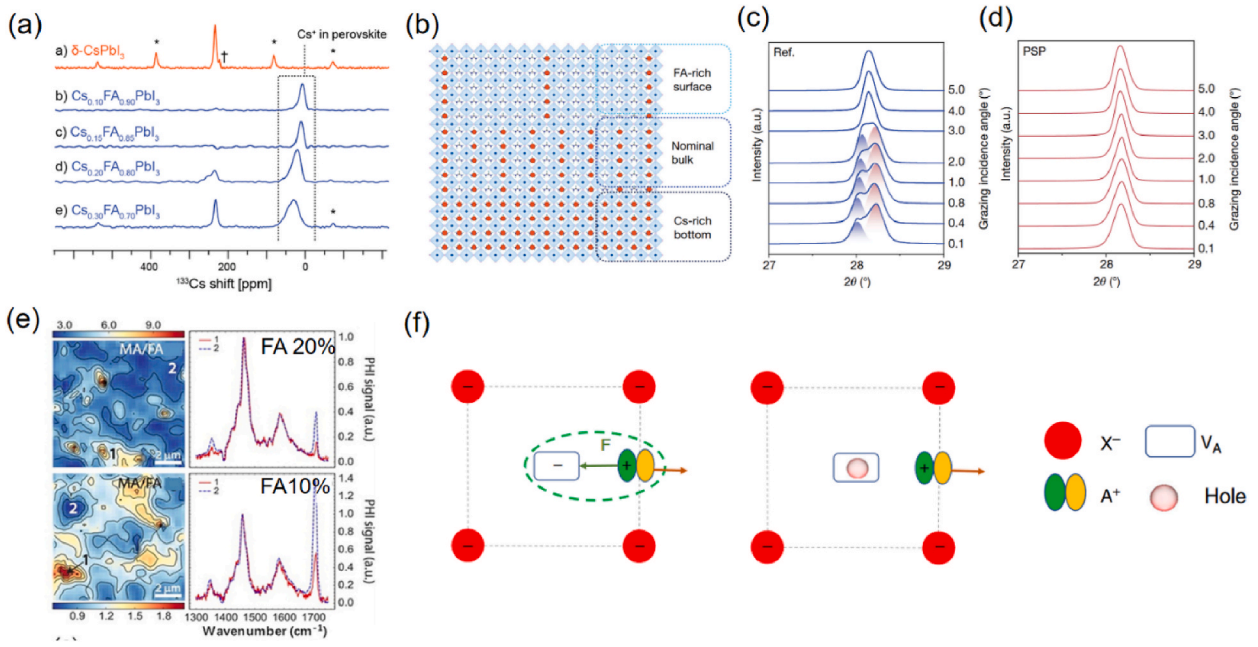

Fig. 3. (a) Quantitative Cs MAS NMR spectra of Cs-FA based perovskite systems [36]. Copyright 2017 American Chemical Society. (b) Schematic illustration of FA-Cs containing perovskites phase segregation in out-of-plane. GIXRD spectra obtained from the bottom layer of (c) the Ref. and (d) the PSP-added FA-Cs perovskite films [37]. Copyright 2023 Springer Nature. (e) Normalized false color MA/FA ratio maps and IR-PHI spectra obtained at the labeled regions for $FA_{0.2}MA_{0.8}PbI_3$ and $FA_{0.1}MA_{0.9}PbI_3$ films [40]. Copyright 2018 American Chemical Society. (f) Schematic mechanism of excessive holes accelerating cation migration [42]. Copyright 2018 Springer Nature.

peak position, which implies that the excess hole would accelerate the cation migration. E_a determined from the temperature-dependent conductivity measurement can directly estimate how easily ions can move inside the perovskite film [43,44], comparing $MAPbI_3$ perovskite films covered by PTAA, PCBM, and PS under the white light with the intensity of 25 mW/cm^2 and a small constant electric field of 0.2 V μm^{-1} [45]. The calculated E_a in these three conditions are 0.035 eV, 0.041 eV, and 0.12 eV, respectively. Both PCBM-covered and PTAA-covered perovskite films have significantly lower E_a values than that of the PS-covered perovskite film, which quantitatively proves that excess electrons or holes lead to ion migration. The influence of the excess charge-induced ion migration in the perovskite film is further envisioned with the help of energy-dispersive X-ray (EDX) and photothermal-induced resonance to identify MA and I at the atomic level during electrical poling. A proposed mechanism for the excess carrier-induced ion migration is shown in Fig. 3f. When ion migration occurs in the perovskites, the energy barriers for the ion migration originate from the Coulombic attraction induced by migrated ions and ion vacancies. When there are excessive light-generated or current-injected carriers in the perovskite film, these carriers can counterbalance the ion vacancies and then reduce the force between the migrated ions and the vacancies, facilitating the ion migration. Regarding the A-site cation migration, the negatively charged cation vacancies (V_A) are generated after the A-site cation migration. V_A can be neutralized by the excessive charge carriers, which weakens the Coulombic attraction between the A-site cation and V_A, thus accelerating the cation migration. As a result, the excessive charge carrier is found to boost ion migration and be one of the decisive restrictions for the stability of mixed A-site cation perovskite-based optoelectronic devices. From the device-level perspective, Abate et al. provided direct evidence of the evolution of the ion migration within the perovskite films sandwiched between the electron and hole selective contacts under device working conditions (Fig. 4a) [46]. The initial schematic represents the stoichiometric amount of anion and cation randomly distributing in the

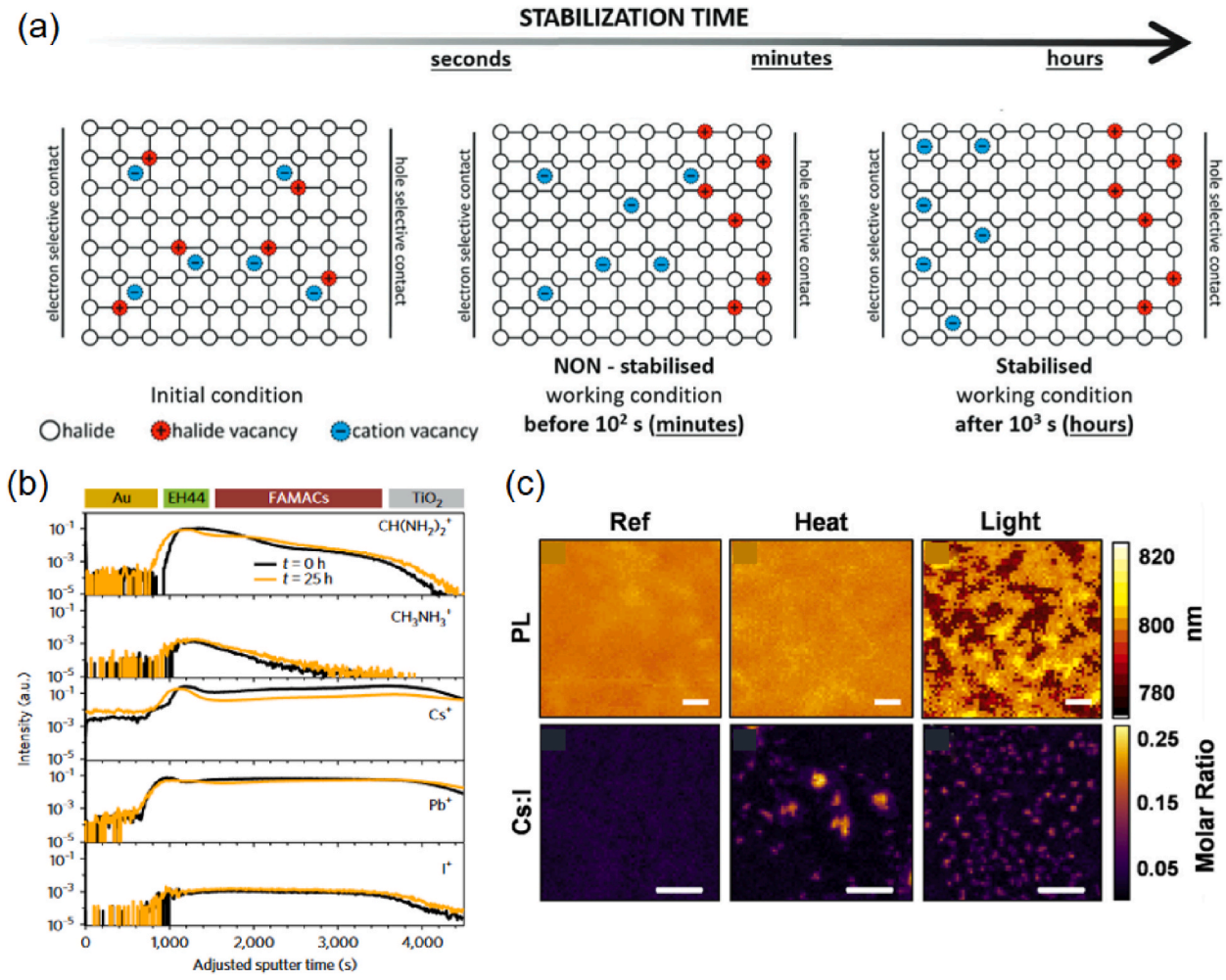

Fig. 4. (a) Schematic diagram of the evolution of the cation and anion distribution within the perovskite layer at different stabilization times under device operational conditions [46]. Copyright 2017 Royal Society of Chemistry. (b) TOF-SIMS profiles of a triple-cation (FA, MA, and Cs) perovskite device before (black) and after (yellow) illumination under 25 h operation time [48]. Copyright 2018 Springer Nature. (c) The PL mapping (top) and XRF mapping (bottom) of $FA_{0.9}Cs_{0.1}PbI_3$ devices that are subjected to Ref, Heat, and Light stressing conditions [49]. The scale bar is 5 μm. Copyright 2020 Elsevier.

perovskite lattice as suggested by Wei et al. (Fig. 4a, left) [47]. After the perovskite film is exposed to the light for up to 10^2 s, halide vacancy migration leads to the form of a Debye layer at the interface with hole selective contact, leaving the cation vacancies (Fig. 4a, middle). In operating conditions with a time longer than 10^3 s, the cation vacancies form an additional Debye layer at the interface with the electron-selective contacts, hindering charge extraction at the interface (Fig. 4a, right). When the perovskite films are put in the dark for several hours to recover, the ionic distribution reverts to the initial stage. However, once the perovskite films are exposed to real operating conditions, slow cation migration becomes irreversible in the device on the hours-timescale. The huge differences in the value of E_a for migration of halide and cation vacancies indicate that hours-ordered-stabilization times are necessary for the perovskites films to reach true stable working conditions. For actual operating devices, Luther et al. conducted time-of-flight secondary ion mass spectrometry (TOF-SIMS) measurements to investigate the compositional distribution and ion migration associated with TiO_2/FAMACs-perovskite/hole transport layer (HTL)/Au device degradation, allowing a component profile to be created for the light-induced spatial change of a triple-cation perovskite device under continuous operation for several hours [48]. After 25 h of the operation, there is no remarkable difference in the distribution of halides and MA. However, obvious redistribution of FA and Cs is discovered (Fig. 4b). Specifically, the Cs migrates particularly to the interface between the perovskite and the HTLs. Nevertheless, the cation redistribution is not observed in the case of utilizing SnO_2 instead of TiO_2 as an electron transporting layer (ETL). For a better understanding of the different results of this cation redistribution between TiO_2 and SnO_2 ETL layers, EQE analysis of before- and after-operated devices with each ETL layer was performed. Post-operated devices with TiO_2 exhibit lower EQE than pre-operated devices in wavelengths shorter than 500 nm. This suggests that the recombination at the TiO_2/FAMACs-perovskite interface increases. On the other hand, post-operated devices with SnO_2 show an almost constant decrease of EQE across the spectrum, implying that the charge separation at the ETL is not affected with SnO_2 contrary to TiO_2. To quantitatively analyze the specific component segregation in the perovskite films, Zhou et al. assessed the spatially optical and elemental distribution of $FA_{0.9}Cs_{0.1}PbI_3$ devices after external stresses such as light and heat utilizing PL-mapping and X-ray fluorescence (XRF) measurements (Fig. 4c) [49]. The PL mapping image within the illuminated device provides clear spatial inhomogeneity where FA-rich (yellow regions of PL image) and FA-poor (brown regions of PL image) phases within the perovskite are seen compared to the Ref. and heat-treated sample. For the elemental distribution, the Cs:I stoichiometric ratio of Ref. is homogeneous without any external stress, but inhomogeneous Cs-rich clusters appear in both heat and light-stressed perovskite devices. The size of Cs-rich clusters becomes larger when treated with thermal stress (85 °C), while the number of Cs-rich clusters increases in the light-stressed perovskite device. Cs-rich clusters are current-blocking and photo-inactive via X-ray-beam-induced current-poor regions. It is worth noting that mixed A-site cation segregation in the perovskite devices can be deteriorated due to thermal and illumination stressing. Few studies have been reported on A-site cation segregation in mixed-cation based PeLED devices compared to mixed halide-based PeLEDs. As we have discussed here, A-site cation segregation can be formed by the external stresses, which hinders continuous and high color-purity of EL emission during the operation. Therefore, studies on A-site cation segregation in PeLED devices should also be pursued more deeply for the long-term stability of PeLED devices.

2.2. *Uniformity of B-sites (Pb-Sn alloyed perovskites)*

As mixing B-site metal cations significantly affects bandgaps, Pb-Sn alloyed perovskites have been recently explored as narrow bandgap absorbers in all-perovskite tandem solar cells (Fig. 1d) [50–54]. Adding Sn into Pb has a “bandgap bowing” effect where the bandgap decreases first but increases at a specific ratio of Sn/Pb. For instance, when $MAPbI_3$ with a bandgap of 1.55 eV and $MASnI_3$ with a 1.35 eV bandgap are mixed, the bandgap decreases to 1.1 eV at 50 % and 75 % of Sn/Pb ratio, not linearly decreasing from 1.55 eV to 1.35 eV [55]. There are two explanations for the bandgap bowing effect [56,57]. First, the bandgap bowing is attributed to competition between spin-orbit coupling (SOC) and lattice distortion [56]. The bandgap decreases because of the dominant SOC effect from heavier Pb atom and lighter Sn atom in $x < 0.5$ (Sn-rich) in $MAPb_xSn_{1-x}I_3$. When $x > 0.5$ (Pb-rich), phase transition from *P*4*mm* space group (α phase) to *I*4*cm* space group (β phase) occurs by $[BI_6]^{4-}$ octahedral rotation. Difference in lattice distortion between the Pb-I-Pb angle (~163.55°) in $MAPbI_3$ and the Sn-I-Sn angle (177.4°) in $MASnI_3$ induces the octahedral rotation. Linear M-I-M (M: metal) angle maximizes *p*-orbital overlap, resulting in a narrower bandgap. The other explanation of the bandgap bowing is the energy mismatch between Pb and Sn orbitals [57]. Since *s* and *p* orbitals of Sn are weakly bounded compared to the counterparts of Pb, the CBM is obtained from the interaction between *s* orbitals of Pb and *p* orbitals of I, while the VBM originates from the *s* orbitals of Sn and *p* orbitals of I. As a result, the bandgap of Pb-Sn alloyed perovskite films decreases even more than that of pure Pb and Sn perovskite films. Based on the interesting bandgap bowing effect, the phase uniformity of Pb and Sn alloys is essential to achieve uniform optoelectronic properties with a narrow bandgap.

As explained in Introduction section, E_a in B-site metal cations is relatively high compared to A-site cations and X-site halide ions. Therefore, phase separation of Pb-Sn alloyed perovskite films induced by external stresses such as electric field, heat, and light is more difficult to form. However, Sn based perovskites have a critical issue of Sn oxidation from Sn^{2+} to Sn^{4+}, which induces low stability, high defect density, short carrier lifetime, and diffusion length in Sn perovskite films [58]. Moreover, this Sn oxidation induces phase non-uniformity in Pb-Sn alloyed perovskite films with uneven optoelectronic properties, so Sn oxidation should be suppressed for the phase uniformity in Pb-Sn alloyed perovskite films. Since Sn oxidation occurs at perovskite surfaces generating Sn^{4+} and Sn^0, not in bulk region of perovskites [59], many antioxidant additives have been reported to suppress Sn oxidation at the perovskite surface [60–66]. Among the several strategies, SnF_2 is an essential reducing agent in Sn-containing perovskite optoelectronics to efficiently decrease Sn oxidation [60,61]. Moreover, the SnF_2-pyrazine complex was utilized to reduce SnF_2 aggregation at the perovskite surface, and hydroxybenzene sulfonic acid was also introduced to maximize the SnF_2 effect [62,63]. In PeLED research fields, additives of phenylethylammonium iodide (PEAI), tryptophan, glycine, 5-aminovaleric acid (5AVA), and Vitamin B1 have been reported with SnF_2

to further enhance Sn chemical stability [64,65]. Research on reducing agents and assistant additives that suppress Sn oxidation can enhance the phase uniformity in Pb-Sn alloyed perovskite films.

Such a fragile Sn oxidation happens even during perovskite crystallization. In its precursor solution, Sn^{2+} is oxidized to Sn^{4+}, inducing high defect density in perovskite crystals after the crystallization (Fig. 5a) [52]. Tan et al. developed the tin-reduced precursor (TRP) method to add metallic Sn into a precursor solution to prevent Sn oxidation in the precursor solution. TRP can lead to spontaneous Sn reduction from even oxidized Sn^{4+} to Sn^{2+} in the solution since reaction Sn + Sn^{4+} -> $2Sn^{2+}$ has a negative Gibbs energy. Metallic Sn removes Sn^{4+} in the solution, and the remaining metallic Sn is filtered by polytetrafluoroethylene 0.2 μm right before the film deposition. The Pb-Sn alloyed perovskite film made by TRP has a strong PL intensity due to decreased non-radiative recombination, resulting in charge carrier lifetimes and diffusion lengths increasing from 3.0 ns to 43.2 ns and from 0.75 μm to

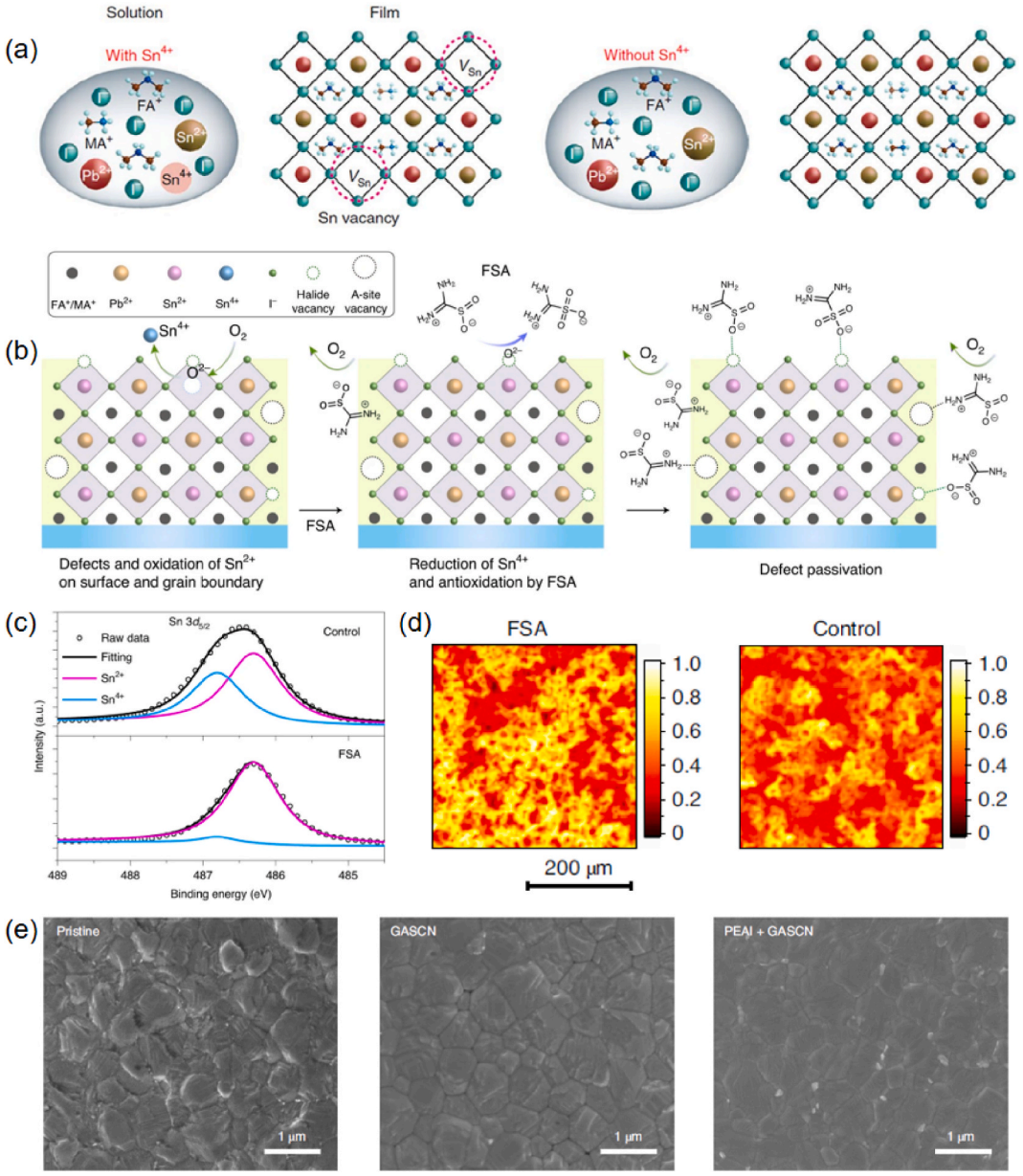

Fig. 5. (a) Schematic diagram of the formation of Sn vacancy because of the presence of Sn^{4+} in the precursor solution and suppressed Sn vacancy due to reduced Sn^{4+} in the metallic Sn containing-precursor solution [52]. Copyright 2019 Springer Nature. (b) Schematic illustration of defect passivation and antioxidation of Sn^{2+} on surface and grain boundary in $FA_{0.7}MA_{0.3}Pb_{0.5}Sn_{0.5}I_3$ perovskite film using FSA. (c) Sn $3d_{5/2}$ XPS spectra of the control and FSA-containing perovskite films after air exposure for 10 min. (d) PL mapping of the FSA-containing and the control perovskite films [53]. Copyright 2020 Springer Nature. (e) Scanning electron microscopy (SEM) images of $(FASnI_3)_{0.6}(MAPbI_3)_{0.4}$ perovskite films without additive (pristine), with only GASCN 7 %, and with both PEAI 2 % and GASCN 7 % [54]. Copyright 2022 Springer Nature.

2.99 μm, respectively. Now, this TRP method has been widely utilized in Sn-containing perovskite optoelectronics [53,64,65,67,68]. In addition, utilization of a Zwitterionic antioxidant has a synergetic effect with the TRP to effectively suppress Sn oxidation in a Pb-Sn alloyed perovskite film. Formamidine sulfinic acid (FSA), a zwitterionic antioxidant, is added in the precursor solution with metallic Sn powder so that Sn oxidation at the Pb-Sn alloyed perovskite surface is decreased (Fig. 5b) [53]. A precursor solution with FSA and without Sn powder remains a yellow color after exposure to air for 5 min, while the color of another precursor solution without both FSA and Sn powder is changed from yellow to red because of Sn oxidation of the precursor solution. Consequently, FSA has a synergy effect with Sn powder in the precursor solution as an antioxidant. In addition, FSA passivates both electron-donating and -accepting defects, having decreased electron and hole trap densities from space charge limit current measurement. As a result, FSA increases PL intensity over three times as decreasing non-radiative recombination, and carrier lifetime from 64 ns to 188 ns due to suppressed carrier trapping. Furthermore, the FSA-containing perovskite film has higher air-stability than the control perovskite film. In $3d_{5/2}$ (~486 eV) X-ray photoelectron spectroscopy (XPS) spectra, Sn^{4+} ratio is significantly decreased in the FSA-containing perovskite film compared to the control perovskite film when exposed to air for 10 min (Fig. 5c). In addition, FSA coordinates with the precursor constituents and is less volatile, retarding perovskite crystallization. The slow crystallization improves phase uniformity in the Pb-Sn alloyed perovskite film, showing uniform EL emission as well as uniform PL mapping, depicted in Fig. 5d.

In addition to Sn oxidation, a difference in crystallization rates between Sn and Pb-based perovskites also leads to non-uniformity in morphology. Sn perovskite crystallization has a smaller nucleation center and faster growth due to stronger covalent interactions between Sn and iodine than the Pb counterpart [69–71], which can inhibit phase uniformity of Pb-Sn alloyed perovskite films. On the other hand, chlorides retard perovskite crystallization kinetics by forming an intermediate phase but not alloying with iodides, and the chlorides are vaporized during thermal annealing [72–75]. Therefore, chlorides can slow down the fast crystallization of Sn perovskites in Pb-Sn alloyed systems. Since the slow crystallization enlarges perovskite grain sizes and smooths surface morphology, chlorides have been widely used in various perovskite optoelectronics [51,76–78]. For instance, 2.5 % chloride addition into a Pb-Sn alloyed perovskite film increases perovskite grain size, crystallinity, and carrier mobility, and it decreases electronic disorder and trap-assisted recombination [51]. With regard to morphology control using additives, Zhu et al. reported that 7 % guanidinium thiocyanate (GASCN) in a Pb-Sn alloyed perovskite film removes pinholes and makes grain boundaries more compact [50]. The enhanced morphology reduces defect density 10 times, leading to carrier lifetime of over 1 μs and diffusion length of over 2.5 μm. Furthermore, the same research group utilized PEAI 2 % and GASCN 7 % to form 2D $(PEA)_2GAPb_2I_7$ ($n = 2$) in a Pb-Sn alloyed perovskite film [54]. The film morphology with the 2D perovskite is smoother and has less clear grain boundaries (Fig. 5e). The 2D

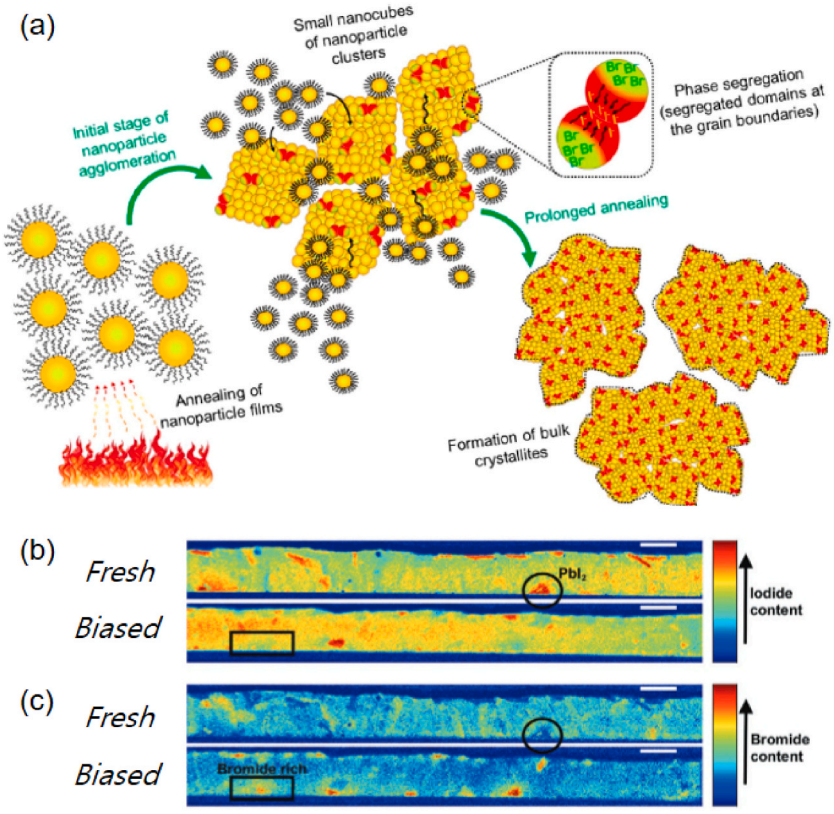

Fig. 6. (a) Schematic illustration of the nanoparticle-to-bulk transformation and halide segregation of $CsPbBr_{3-x}I_x$ perovskites under annealing process [92]. Copyright 2018 American Chemical Society. NMF loadings (maps) of selected components, with the fresh and biased samples about elemental distribution of (b) iodide and (c) bromide [98]. All scale bars are 0.5 μm. Copyright 2020 Wiley.

perovskite located at the perovskite surface passivates defects and reduces dark carrier density 1000 times. Morphology control can prevent Sn oxidation at the perovskite surface, which is a critical aspect to fabricate uniform Pb-Sn alloyed perovskite films.

Sn-based PeLEDs have been in spotlight since 2023 owing to emitting NIR range of ~900 nm with high EQE of ~10 % and brightness [64–66]. Utilizing strategies of TRP, PEA addition, etc. mentioned above, Sn-based PeLEDs have been developed following development of Sn perovskite solar cells (PeSCs). However, research on Pb-Sn alloyed PeLEDs is still lacking. The Pb-Sn alloyed PeLED should be explored in the future because of the bandgap bowing effect of Pb-Sn alloyed perovskite films with an NIR range deeper than

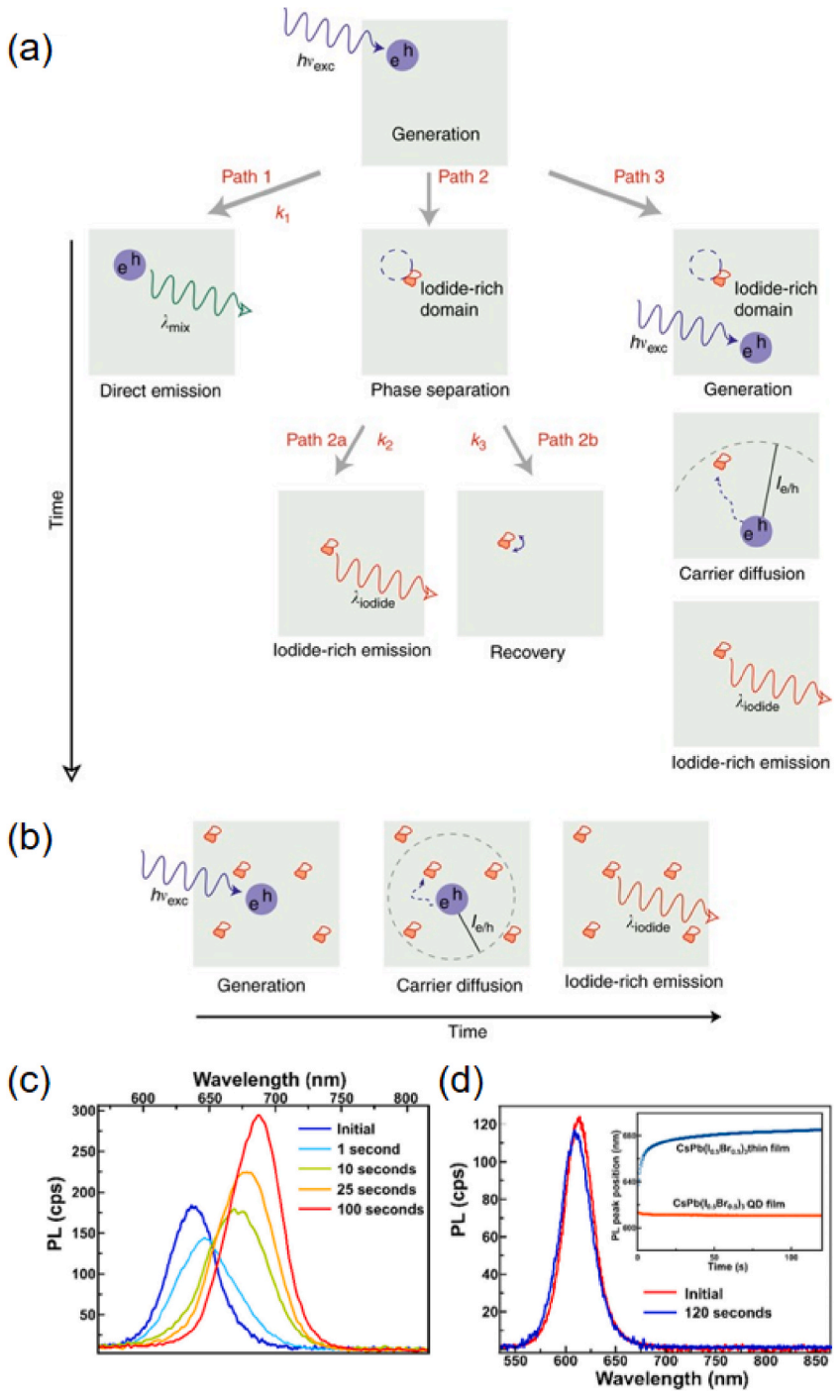

Fig. 7. Schematic images of kinetic processes during halide phase segregation under (a) low and (b) high intensity of light. PL emission spectra of (c) thin film, and (d) NC under 405 nm continuous light illumination [82]. Copyright 2017 Springer Nature.

1000 nm. The phase non-uniformity of Pb-Sn alloyed perovskite films can induce non-uniform EL emission, which would be the most critical issue for the deep NIR PeLED composed of Pb-Sn alloys.

2.3. X-site halide segregation

Halide segregation is a major segregation phenomenon in PeLEDs, which significantly hinders the essential characteristic of selective wavelength light emission. Therefore, halide segregation must be suppressed to ensure high wavelength selectivity and stability in luminescence of PeLEDs, which are crucial requirements for real commercialization. Several strategies have been suggested to mitigate halide segregation in PeLEDs. These include increasing grain size and crystallinity of perovskite films to reduce defect density [79–81], decreasing the particle size of quantum dots or nanocrystals (NCs) [82], implementing defect passivation [83], partially substituting Pb with Sn [84], applying external pressure [85], alloying Cl into the I/Br lattice [86], and alloying A-site cations [87–90]. However, the majority of research in this area has been predominantly reported on PeSCs, despite the active exploration for PeLEDs [81,83,91]. Here, we aim to review the mechanism of halide segregation and strategies for suppressing halide segregation in both PeSC and PeLED devices.

2.3.1. Mechanism of halide segregation

The origin of halide segregation can be broadly categorized into three main factors, including heat [92–94], electrical bias [95–99], and light exposure [82,93,94,100,101]. First, for the heat-induced halide segregation, mixed halide perovskites often exhibit a tendency to form halide segregation, which is thermodynamically more stable than uniform halide distribution under the heat. Mora-Seró et al. proposed a mechanism for halide segregation during the thermal annealing process of $CsPbBr_{3-x}I_x$ perovskite NCs (Fig. 6a) [92]. Most long-chain organic ligands are depleted during thermal annealing, leading to $CsPbBr_{3-x}I_x$ NCs growth into larger particles with a nanocube shape. The nanocubes, in turn, promote halide segregation at grain boundaries under light irradiation. As a result, distinct PL emissions from Br-rich and I-rich domains increase as the size of the nanocubes increases, while green PL emission that indicates well mixed-halides decreases. In other words, the halide segregation dominantly occurs in large nanoparticles rather than small nanoparticles. Consequently, they suggested that reducing particle sizes could effectively suppress the halide segregation and may contribute to improved performance of the mixed-halide perovskite based optoelectronic devices. Second, for the bias-induced halide segregation, Cl^-, Br^-, and I^- halide ions primarily migrate towards the electrode under bias, resulting in halide segregation, with the smaller-sized ion reported to segregate more prominently due to lower hindrance compared to the bigger-sized ions [95–99]. Abate et al. demonstrated a clear visualization of bias-induced halide segregation in optoelectronic devices using EDX spectroscopic data analyzed with non-negative matrix factorization (NMF) [98,102]. The fresh perovskite layer in the device displays the expected presence of both iodine and bromine components. Nevertheless, under a bias in the dark, a noticeable halide ion movement and halide segregation occur, resulting in the iodine-rich phase becoming more predominant in the bulk of the perovskite layer (Fig. 6b). Additionally, small bromine-rich areas emerge at the bottom interface (Fig. 6c). As a result, the decrease in short-circuit current density (J_{SC}) and fill factor (FF), leading to the loss of power conversion efficiency (PCE), could be explained by charge trapping from iodide-rich domains, degradation at the interfaces, and poor charge transport and collection due to the low conductivity of the amorphized perovskite [98].

Third, for photo-induced halide segregation, the diffusion of photo-generated carriers induces halide segregation [82,100]. Kuno et al. reported a strategy to reduce halide segregation through the utilization of perovskite NCs [82]. The research article highlights that the diffusion of photogenerated carriers is a primary cause of halide segregation, and suppressing the diffusion length of the photogenerated carriers is an effective method to prevent halide segregation. Fig. 7a provides a schematic illustration of a kinetic model for light-induced halide segregation in $MAPb(I_{0.5}Br_{0.5})_3$ with a PL emission wavelength of 652 nm. Initially, the mixed-halide perovskite layer absorbs light, generating photogenerated excitons (electron-hole pairs) (Fig. 7a, top). Subsequently, some of the photogenerated carriers, as illustrated in Path 1, undergo the recombination process to directly emit light at the wavelength of 652 nm. However, as depicted in Path 2a, photoexcitation induces a driving force for local halide anion rearrangement, leading to the formation of iodide- and bromide-rich domains, followed by the emission of light from the iodide-rich phase. The iodide- and bromide-rich domains are thermodynamically recovered (Path 2b), but at a much slower rate than Path 2a, ultimately resulting in the persistence of both iodide- and bromide-rich domains. In addition, photogenerated carriers diffuse to the halide segregation regions, leading to light emission from the iodide-rich domains, as shown in Path 3. In this manner, photoexcitation induces halide segregation, resulting in a red shift of the emission wavelength in the mixed halide perovskite. This phenomenon becomes more predominant when the concentration of photogenerated carriers increases, leading to a higher probability of the formation of the halide segregation. Moreover, photogenerated carriers easily diffuse to the high density of halide segregation regions under high-intensity light emission (Fig. 7b). To reduce the redshift by suppressing the diffusion of photogenerated carriers, $CsPb(I_{0.5}Br_{0.5})_3$ NCs are introduced instead of $CsPb(I_{0.5}Br_{0.5})_3$ thin film. The thin film initially exhibits PL emission at 637 nm, but the PL peak is shifted to 687 nm after 100 s due to the halide segregation under light at 405 nm with an intensity of 60 mW/cm^2 (Fig. 7c). On the other hand, the NCs show a minimal blue-shift (only 3 nm) of the PL peak under the same condition (Fig. 7d). This shift is attributed to perovskite degradation under ambient conditions rather than the halide segregation. Therefore, the introduction of NCs can effectively suppress halide segregation.

2.3.2. Halide segregation in PeSCs

PeSCs are one of the most actively researched devices in the field of perovskite-based electronic devices, with many studies developed for PeSCs being applied to other devices such as LEDs and transistors [103–106]. Accordingly, in this review, we briefly highlight studies that have effectively suppressed halide segregation in PeSCs. Various strategies have been attempted to minimize

halide segregation in mixed halide PeSCs: compositional engineering [84,107,108], defect passivation [109,110], and alloy formation of 2D/3D perovskites [83,111]. Jen et al. reported the development of highly efficient and stable PeSCs by introducing a small amount of Sn into $MAPb(I_{0.6}Br_{0.4})_3$ for suppressing halide segregation [84]. The photocurrent density of $MAPb(I_{0.6}Br_{0.4})_3$ based PeSCs steadily decreases from 13.16 to 7.08 mA cm^{-2} during 1 sun illumination for only 300 s as shown in Fig. 8a, indicating increased trap-assisted recombination as a new combination of the perovskite composition with smaller bandgaps (I-rich domain) is formed under illumination. On the other hand, $MAPb_{0.75}Sn_{0.25}(I_{0.6}Br_{0.4})_3$ PeSCs exhibit a consistent photocurrent density of 15.69 mA cm^{-2} under 1 sun illumination for over 2 h, providing evidence for their high compositional stability under the illumination (Fig. 8b). The difference in the absolute current densities of the two kinds of PeSCs is originated from a narrower bandgap due to the Sn incorporation. In transient absorption spectra (TAS) analysis, a new photobleaching peak emerges from 700 to 800 nm (I-rich) and the original photobleaching peak from $MAPb(I_{0.6}Br_{0.4})_3$ is shifted from 660 nm to 560–640 nm (Br-rich), however there is no significant peak shift in $MAPb_{0.75}Sn_{0.25}(I_{0.6}Br_{0.4})_3$. This result clearly indicates that $MAPb(I_{0.6}Br_{0.4})_3$ undergoes phase separation into Br-rich and I-rich phases, and the incorporation of Sn could give critical roles for contribution of the stabilization of the I/Br mixed system under illumination. McGehee et al. demonstrated the bandgap tuning of perovskite materials by increasing Cs ratio in $Cs_xFA_{1-x}Pb(Br_yI_{1-y})_3$ instead of increasing Br ratio to suppress halide segregation [107]. Each of the high ratios of Cs and Br in the perovskite film has a similar effect to widen the bandgap, leading to an increase in V_{oc}, followed by optimizing the ratio of Cs and Br to achieve a high PCE. The perovskite

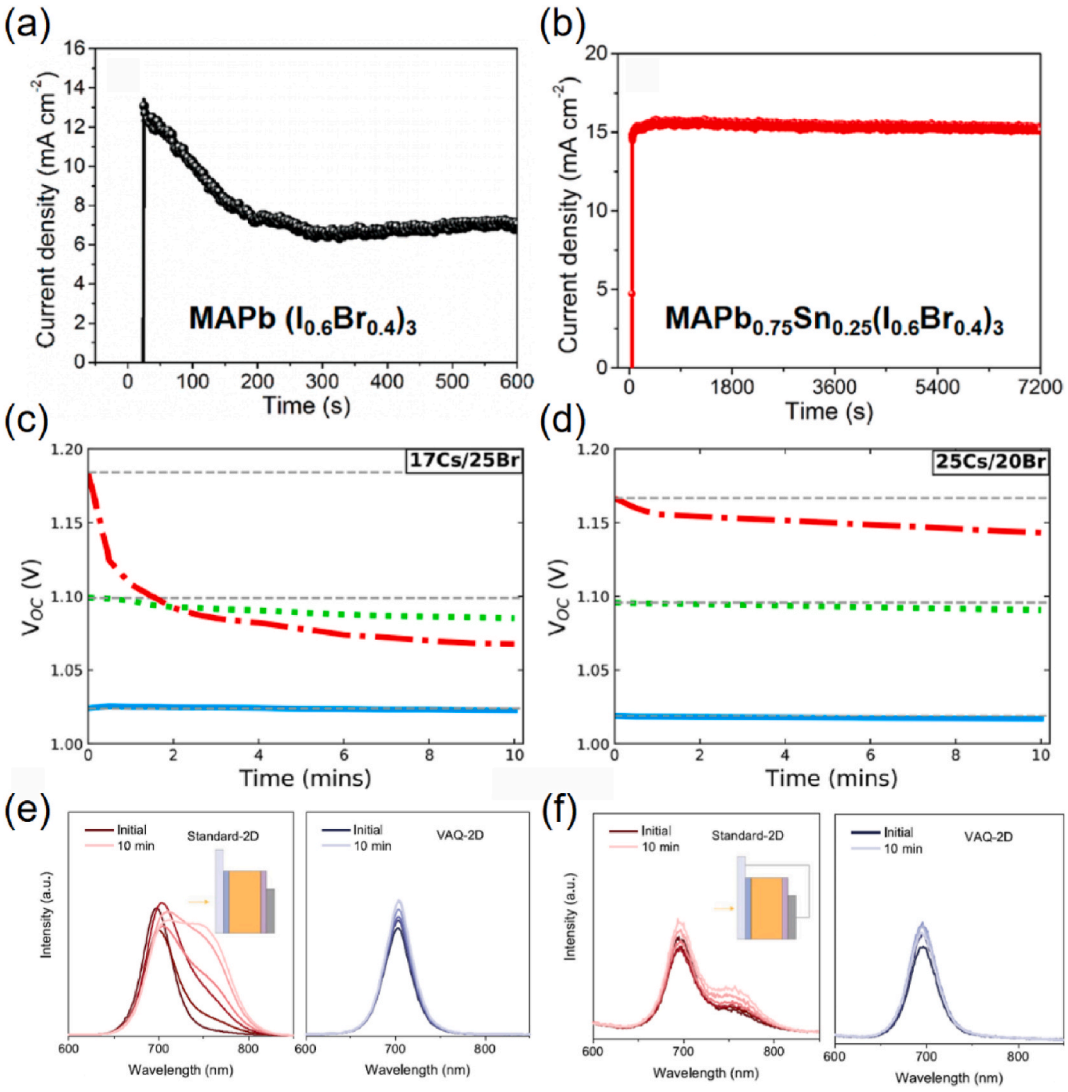

Fig. 8. Steady-state photocurrent measurement of (a) $MAPb(I_{0.6}Br_{0.4})_3$ and (b) $MAPb_{0.75}Sn_{0.25}(I_{0.6}Br_{0.4})_3$ PeSCs with an applied voltage of 0.86 and 0.74 V at the maximum power point, respectively [84]. Copyright 2016 American Chemical Society. V_{oc} monitoring of PeSCs under light illuminations based on (c) $Cs_{0.17}FA_{0.83}Pb(Br_{0.25}I_{0.75})_3$ and (d) $Cs_{0.25}FA_{0.75}Pb(Br_{0.2}I_{0.8})_3$ perovskite films [103]. Copyright 2018 American Chemical Society. PL spectral evolution of standard-2D and VAQ-2D devices under (e) open-circuit and (f) short-circuit condition with a 532 nm laser excitation (intensity equivalent to 15 suns) for 10 min [107]. Copyright 2018 American Chemical Society.

films with a higher Cs ratio (25 % and 40 %) at the A-site have a negligible PL peak shift regardless of Br ratio (20 % and 30 %), while the perovskite films with lower Cs ratio of 17 % (noted as 17Cs) have huge redshifts in PL spectra under various conditions of light exposure. When Br ratio increases from 25 % to 40 % in 17Cs, the redshift of PL spectra increases to over 70 nm after 10 sun for 10 min, which is attributed to halide segregation. In the PeSCs with high Cs and low Br compositions, the decrease in V_{oc} during the PL measurements is less pronounced, indicating much more photo-stable V_{oc} (Fig. 8c and d). Therefore, adding Cs rather than Br in the perovskite film can contribute to higher V_{oc} with high photo-stability in PeSCs. Based on the fine tuning of Cs and Br ratio, the PeSCs with 25Cs and 20Br exhibit the highest PCE of 17.4 %.

In addition to compositional engineering, there are studies related to defect passivation that significantly prevent halide segregation by utilizing an electron-donating molecule or K^+ ion into perovskite films [109,110]. McGehee et al. reported that the introduction of the electron-donating trioctylphosphine oxide (TOPO) onto the perovskite layer not only reduces nonradiative recombination but also markedly decreases halide segregation in $MAPbI_2Br_1$ films [109]. They proposed a model of halide segregation

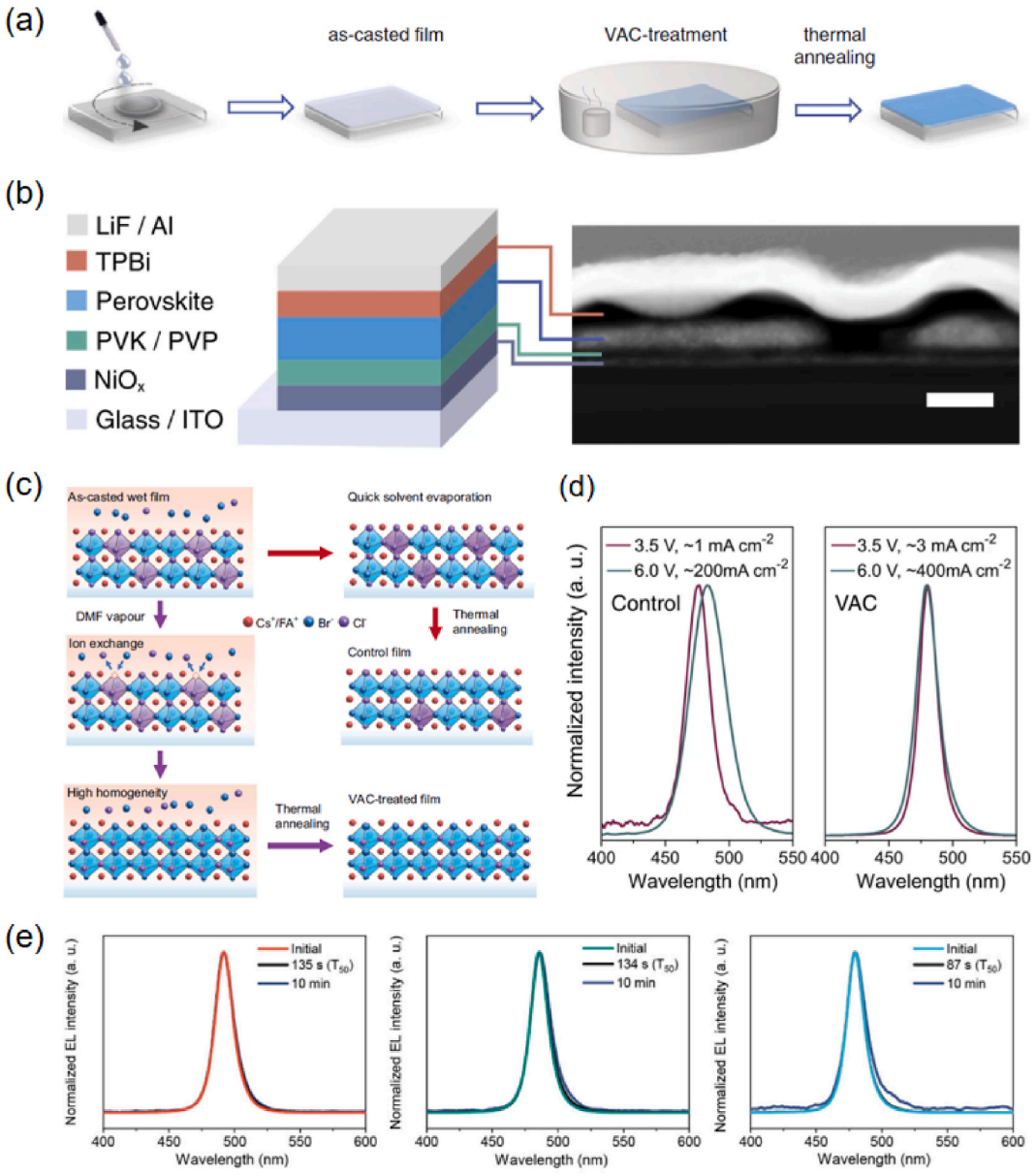

Fig. 9. (a) Schematic image of VAC-based fabrication process of perovskite film. (b) Schematic illustration of the PeLED device architecture and corresponding cross sectional SEM image. (c) Schematic illustration of the proposed mechanism for halide redistribution for conventional and VAC-based fabrication process of perovskite film. (d) Normalized EL spectra of conventional and VAC-treated devices at low voltage (3.5 V) and high voltage (6.0 V). (e) Stable EL characteristics of PeLED for Cl 30 % (left), Cl 35 % (middle), and Cl 40 % (right) devices [81]. Copyright 2021 Springer Nature.

that carrier trapping at surface states induces local electric fields, driving the movement or accumulation of ionic defects, resulting in photoinduced trapping-induced halide segregation. Based on the model, TOPO passivates trapping sites on the surface of the perovskite film, effectively suppressing the halide segregation. Stranks et al. reported that utilizing K^+ ion remarkably functions to suppress halide segregation in I/Br mixed-halide perovskites [110]. K^+ ion highly passivates halide vacancies predominantly formed on the grain surface and induces Br^- ions located at the grain boundaries and I-rich phases in the bulk of the mixed-halide perovskite. The defect passivation at the grain boundaries and halide rearrangement effectively suppress halide ion migration and increase luminescence yield. In addition, the effective prevention of halide segregation is achieved through the introduction of 2D/3D perovskites. Tan et al. reported a new deposition method of hybrid evaporation/spin-coating to introduce 2D/3D perovskites with high n number [111]. One of widely used wide-bandgap 3D perovskites, $Cs_{0.2}FA_{0.8}Pb(I_{0.6}Br_{0.4})_3$, was deposited first, followed by thermal deposition of PbI_2 (10 nm), MAI spin coating, thermal treatment, and PEAI spin coating with subsequent thermal treatment to lead the formation of a 2D perovskite layer with majority of $n = 3$ on the 3D perovskite film (noted as VAQ-2D). On the other hand, a conventional 2D/3D perovskite made by a simple two-step deposition that PEAI spin coating on the 3D perovskite film with subsequent thermal treatment has the majority of the $n = 1$ 2D perovskite (named as standard-2D). To compare light-induced halide segregation under operation conditions of the PeSCs, the PeSCs were exposed to 532 nm laser light with an intensity equivalent to 15 suns for 10 min under open-circuit and short-circuit conditions (Fig. 8e and f). PL spectra from the standard-2D PeSC shows new shoulder peaks with longer wavelengths than the initial PL peak while there is no peak shift in the VAQ-2D PeSC, indicating that the VAQ-2D significantly suppresses halide segregation with high photo-stability. $n = 3$ in the VAQ-2D accelerates charge extraction from the 3D perovskite, while $n = 1$ in the standard-2D induces charge accumulation at the 2D/3D interface. Therefore, dimensional control on 3D perovskites can suppress halide segregation due to a decrease in charge accumulation.

2.3.3. *Halide segregation in PeLEDs*

Halide segregation is an important research topic in PeLEDs. There have been a few strategies to prevent halide segregation and ensure both high EQEs and operational stability in PeLEDs including crystallinity control [81], doping [112–118], and the introduction of a bulky organic cation [83]. For example, Gao et al. reported a deposition method of $CsPb(Br_xCl_{1-x})_3$ perovskite films with high homogeneity and no halide segregation, which is solvent vapor-assisted crystallization (VAC) [81]. Dimethyl sulfoxide (DMSO)-based

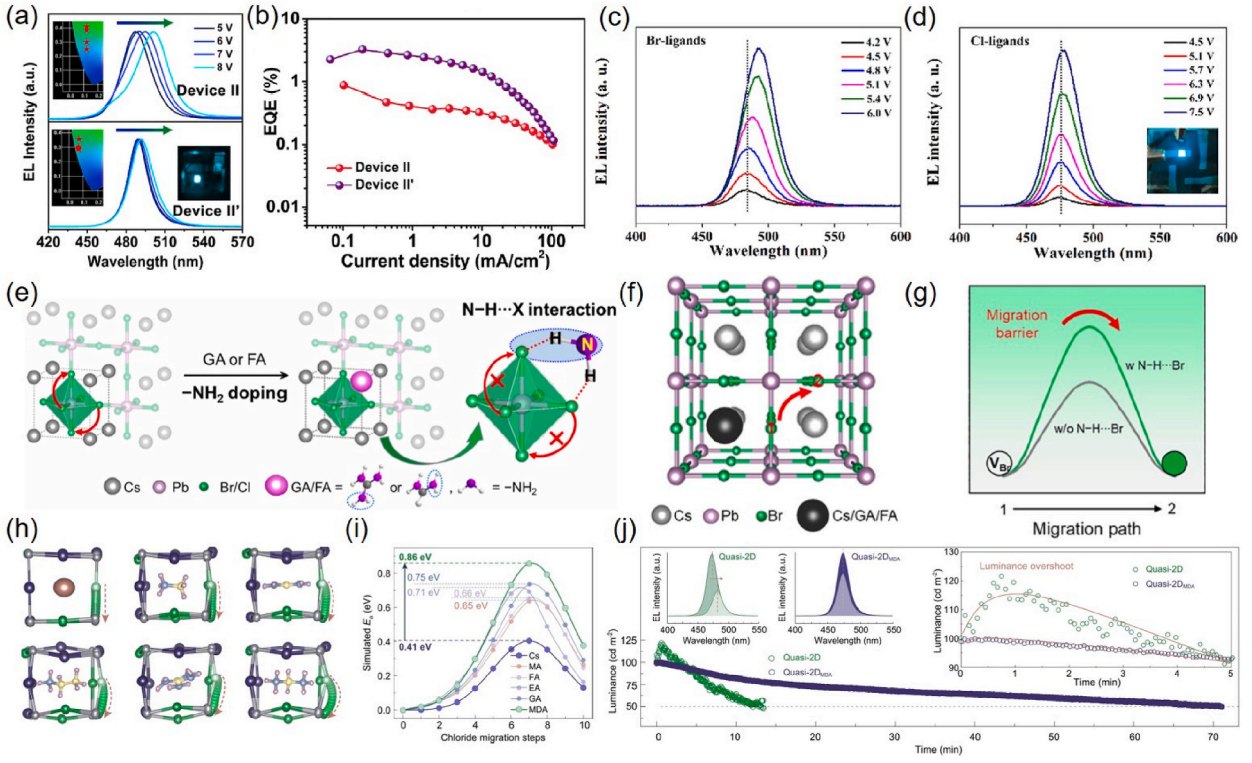

Fig. 10. (a) EL spectra and (b) EQE characteristics of undoped PeLEDs (Device II) and La^{3+}-doped PeLEDs (Device II') [112]. Copyright 2020 Elsevier. EL spectra based on (c) Br-ligands and (d) Cl-ligands derived PeLEDs under varied biases (inset: a photograph of an operating PeLED) [113]. Copyright 2021 Elsevier. (e) Schematic of inhibiting ion migration for $CsPbBr_xCl_{3-x}$ nanocrystals by GA or FA doping strategy. (f) Ion migration pathway via GA or FA doping based N-H···Br interaction. (g) Schematic illustration of the migration barrier from site-1 to site-2 (following the pathway in Fig.10f) with and without N-H···Br interaction [114]. Copyright 2021 Elsevier. (h) Schematic images of top view for chloride migration pathways and (i) theoretically calculated E_a for perovskites substituted by different cations. (j) Operational stability test of the devices with and without MDA doping (left inset: variation in EL spectra, right inset: EL luminance overshoot) [115]. Copyright 2023 Wiley.

precursor solution is spin-coated on a substrate, followed by placing the spin-coated substrate in a Petri dish with a small amount of dimethylformamide (DMF) for approximately 20 min in vacuum, and finally thermal annealed to induce crystallization (Fig. 9a). The device structure of the PeLEDs is glass/ITO/NiO_x/poly(9-vinylcarbazole) (PVK):polyvinylpyridine/perovskite/2,2′,2″-(1,3,5-benzinetriyl)tris(1-phenyl-1H-benzimidazole) (TPBi)/LiF/Al (Fig. 9b). The introduction of VAC establishes an environment conducive to halide rearrangement within the perovskite films, which homogenizes the local chemical composition and minimizes disorder (Fig. 9c). Initially, the as-casted wet film comprises various Cl-rich and Br-rich components in liquid phases, resulting from nonequilibrium crystal growth during spin-casting. Without VAC treatment, the perovskite film experiences rapid solvent evaporation, followed by the immediate fixation of the perovskite composition. While post-annealing provides some alleviation of elemental heterogeneity, the heterogeneity that was initially formed persists partially in the control film. In contrast, the inclusion of DMF vapor allows the preservation of the liquid phase over an extended period. This prolonged liquid phase facilitates the subsequent halide exchange process, driven and modulated by the chemical potential difference between the solid (Cl-rich) and liquid phases (Br-rich). The halide exchange process progressively approaches chemical equilibrium, which ensures a homogeneous distribution of constituents. Because the subsequent thermal-annealing process has minimal influence on the PL spectra of the VAC-treated film, a highly homogeneous composition is already formed during the VAC treatment, leading to almost no shift in EL spectra at different voltages of 3.5 V and 6.0 V (Fig. 9d). The VAC-treated devices with varying chloride content (30 %, 35 %, and 40 %) also have no observable shift in EL spectra after operating for over 10 min (Fig. 9e). Based on well-suppressed halide segregation, the VAC-treated PeLED achieves an EQE value of up to 11.0 % while the control PeLED only achieves 5 % of EQE.

Doping strategies have also been reported for suppressing halide segregation in PeLEDs. Wang et al. reported lanthanum (La) doping for $CsPb(Br_xCl_{1-x})_3$ nanocrystals to achieve highly efficient PeLEDs by suppressing halide segregation [112]. Doping La^{3+} ions into $CsPb(Br_{0.7}Cl_{0.3})_3$ perovskite nanocrystals induces a strong interaction between La^{3+} and Cl^-, which decreases the electron density around Cl^-. As a result, the Cl^- nucleus binds its outer electrons more tightly, leading to an increase in binding energy. The strong interaction between La^{3+} and Cl^- is advantageous in preventing the loss of chlorine, which is favorable for reducing defect density and enhancing the photoluminescence quantum yield (PLQY). Note that the device structure of the PeLEDs is glass/ITO/poly(3,4-ethylenedioxythiophene: poly(styrenesulfonate) (PEDOT:PSS)/PVK/La^{3+}-doped perovskite nanocrystals/TPBi/LiF/Al. The normalized EL spectra of La^{3+}-doped PeLEDs show a minimal shift from 489 nm to 492 nm, in contrast to the more pronounced shift observed in the undoped PeLEDs, which ranges from 487 nm to 501 nm (Fig. 10a). Additionally, the EQE of La^{3+}-doped PeLEDs reaches 3.25 %, while the undoped PeLEDs exhibit an EQE of only 0.84 % (Fig. 10b). These results highlight the effect of La^{3+} doping on suppressing halide migration, resulting in enhanced spectral consistency and device efficiency. As another doping strategy, Duan et al. reported chloride terminated ligands (2-(2-naphthyl) ethylamine hydrochloride, Cl-ligands) to replace the counterpart bromide terminated ligands (2-(2-naphthyl)ethylamine hydrobromide, Br-ligands) to successfully suppress halide segregation in $FAPbBr_{3-x}Cl_x$ thin films, as compared in EL spectra (Fig. 10c and d) [113]. Following ToP-SIMS analysis of PeLEDs based on Cl- and Br-ligands after stressing at 5V for 2 min, the Cl-ligand-based PeLED exhibits significantly suppressed Cl migration compared to its Br-ligand counterpart. While the Br-ligand-based PeLED has Cl-rich surface of the perovskite film, Cl-ligand-based PeLED effectively suppresses the diffusion of internal Cl ions toward the surface.

Zeng et al. reported guanidine (GA) or FA as amine-group (-NH_2) doping for $CsPbBr_xCl_{3-x}$ perovskite nanocrystals to induce strong N-H···Br interaction, leading to less EL shift than without doping system [114]. Fig. 10e presents a schematic illustration of Br migration along the $[PbBr_6]^{4-}$ octahedrons under GA and FA (-NH_2) doping condition with N-H···Br interaction. The mixed cation system exhibits a higher migration barrier compared to $CsPbBr_3$ (simplified system for the calculation) without amine group, indicating that halide migration is effectively suppressed by amine group doping (Fig. 10f and g). As a results, PeLEDs fabricated with an glass/ITO/PEDOT:PSS/PTAA/perovskite film/TPBi/LiF/Al structure achieves EQEs of 4.14 % (FA) and 3.02 % (GA), significantly surpassing the 1.3 % EQE observed in the undoped PeLED, which also exhibits a peak shift in EL spectra from 487 to 502 nm. In contrast, the EL spectra of the doped PeLEDs remain stable, with peak positions at 490.5 nm (GA) and 492.5 nm (FA), showing no noticeable shift. For other types of A cation, Yuan et al. reported that large-scale doping of methylammonium (MDA^{2+}) into $CsPb(Br_{0.6}Cl_{0.4})_3$-based PeLEDs effectively suppresses halide segregation through localized lattice distortion [115]. In theoretical simulation, pure $CsPb(Br/Cl)_3$ perovskites show a predominantly linear migration path for halide ions. However, for all types of substituted mixed cation perovskites, curved migration paths are observed as dominant, following brown arrows in Fig. 10h. This result indicates that after partial substitution at the "A-site," the E_a in Cl-Br mixed perovskites has been increased (Fig. 10i). Among the A-site candidates, the partial substitution of large cations such as MDA and PEA can form quasi-2D perovskites. For the quasi-2D PeLEDs, MDA 10%-incorporated $CsPb(Br_{0.6}Cl_{0.4})_3$ (quasi-$2D_{MDA}$) based PeLED shows a higher EQE of 14.2 % than $4PEA_2Cs_3Pb_4(Br/Cl)_{13}$ (quasi-2D) based PeLED, which achieves an EQE of 10.1 %. Moreover, the quasi-$2D_{MDA}$ PeLEDs maintain stable EL spectra while the quasi-2D PeLEDs exhibit an 18 nm shift in EL spectra under various working voltages (Fig. 10j, left inset), indicating that halide segregation is effectively suppressed by MDA doping. Interestingly, the quasi-$2D_{MDA}$ PeLEDs demonstrates a half-lifetime working stability of 72 min, which is over 5.5 times longer than the quasi-2D device (Fig. 10j). Additionally, other strategies including doping perovskite nanocrystals with $NdCl_3$ [116], introducing cationic surfactants to improve the homogeneity of the precursor solution [117], and introducing 5AVA to effectively passivate the defects of 3D perovskite films [118] have been reported to greatly suppress halide segregation, thereby maintaining stable EL spectrum peaks in PeLEDs.

In addition to crystallinity control and doping strategies, the utilization of long-chain organic cations has been reported to suppress halide segregation by reducing perovskite crystal sizes [83]. The suppression occurs because there is a higher likelihood of halide ion redistribution within a single crystal domain under illumination [119]. Rand et al. reported an addition of n-butylammonium (BA) that $BAI_{1-x}Br_x{-}Cs_{0.6}MA_{0.4}(I_{1-x}Br_x)_3$ shows high photo-stability without halide segregation [83]. In high-resolution transmission electron microscopy (TEM) images, the grain size of the BA-containing perovskite film significantly decreases to approximately 10 nm, while

$Cs_{0.6}MA_{0.4}Pb(I_{0.6}Br_{0.4})_3$ and $MAPb(I_{0.6}Br_{0.4})_3$ films exhibit a grain size of 30–50 nm and 50−100 nm, respectively (Fig. 11a). The nanometer-sized grains formed from the incorporation of the BA shield through halide redistribution. In this case, the energetic and lattice mismatch between I- and Br-rich domains makes halide segregation energetically unfavorable within these nanometer-sized crystallites. To compare light-induced halide segregation of the perovskite films with and without BA, the perovskite films with various Br ratios, including 0 %, 20 %, 40 %, 60 %, 80 %, and 100 %, were subjected to light stress (1 sun illumination in N_2 for 20 min). The light-exposed $BAI_{1-x}Br_x$−$Cs_{0.6}MA_{0.4}(I_{1-x}Br_x)_3$ film exhibits no PL peak shift. In contrast, $MAPb(I_{0.6}Br_{0.4})_3$ and $Cs_{0.6}MA_{0.4}Pb$-$(I_{0.6}Br_{0.4})_3$ films show significant PL peak shifts under all Br ratios except 0 % and 100 % (Fig. 11b–d). Further, PeLEDs based on three different perovskite films are compared in the aspect of halide segregation, which have a device structure of

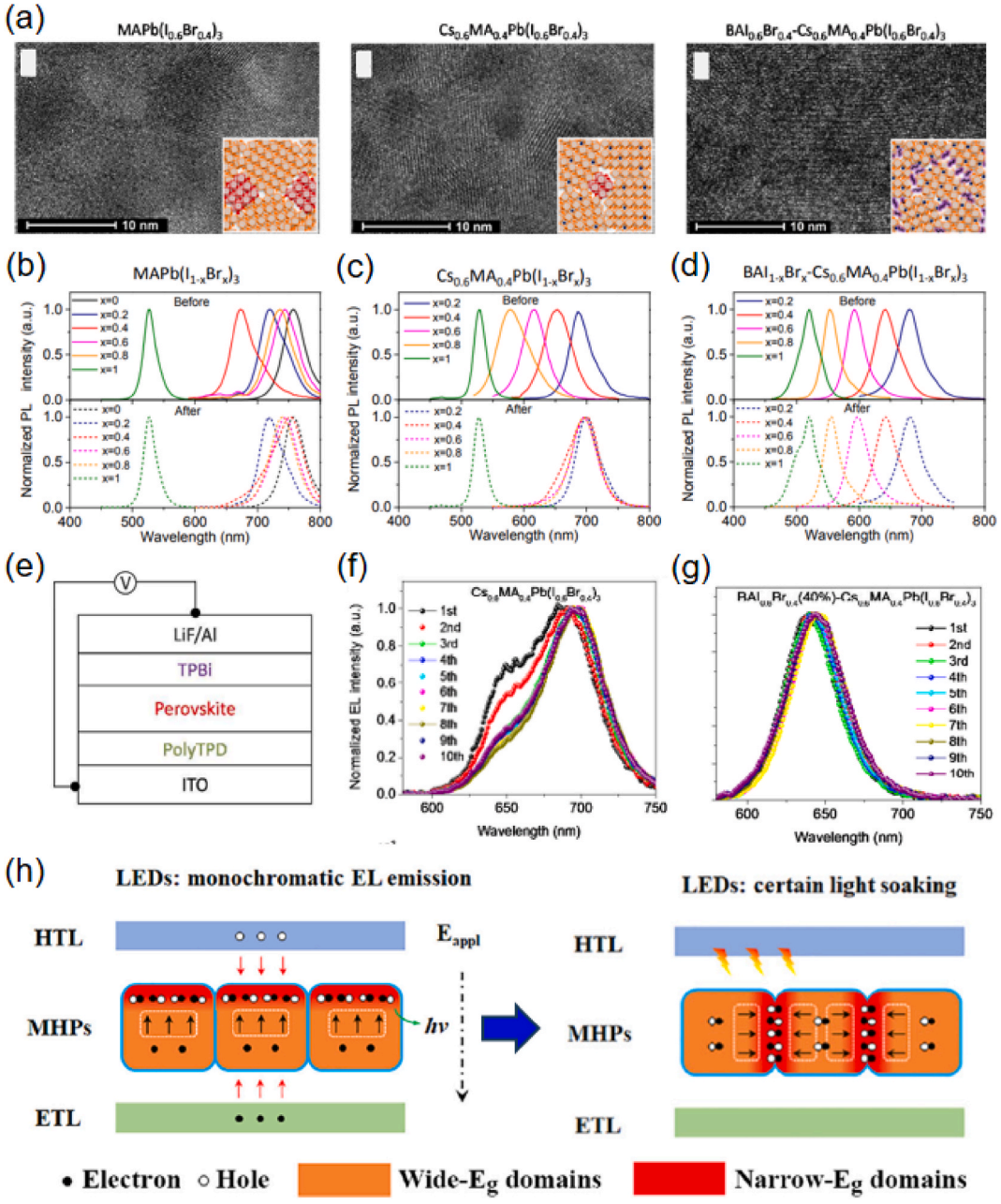

Fig. 11. (a) TEM images and schematic images (inset) of perovskite grains for $MAPb(I_{1-x}Br_x)_3$, $Cs_{0.6}MA_{0.4}Pb(I_{1-x}Br_x)_3$, and $BAI_{1-x}Br_x$-$Cs_{0.6}MA_{0.4}Pb(I_{1-x}Br_x)_3$ perovksite films. Normalized PL spectra of (b) $MAPb(I_{1-x}Br_x)_3$, (c) $Cs_{0.6}MA_{0.4}Pb(I_{1-x}Br_x)_3$, and (d) $BAI_{1-x}Br_x$-$Cs_{0.6}MA_{0.4}Pb(I_{1-x}Br_x)_3$ before and after light illumination. (e) Schematic image of the PeLED device structure and normalized EL spectra of the PeLEDs based on (f) $Cs_{0.6}MA_{0.4}Pb(I_{0.6}Br_{0.4})_3$ and (g) the perovskite layer with 40 % of $BAI_{0.6}Br_{0.4}$ concentration for different scan cycles [83]. Copyright 2017 American Chemical Society. (h) Proposed mechanism and prospective exploitation of halide segregation in the PeLED [91]. Copyright 2023 Elsevier.

Glass/ITO/poly[N,N′-bis(4-butylphenyl)-N,N′-bis(phenyl)-benzidine]/perovskite/TPBi/LiF/Al (Fig. 11e). When x is 0.4 in $BAI_{1-x}Br_x{-}Cs_{0.6}MA_{0.4}(I_{1-x}Br_x)_3$, the highest EQE reaches 5 % for red PeLEDs with a stable EL emission of 650 nm. In addition, the BA-incorporated PeLED exhibits stable EL spectra characteristics even after multiple bias scanning cycles, while the $Cs_{0.6}MA_{0.4}P$-b-$(I_{0.6}Br_{0.4})_3$ PeLED shows redshift of EL spectra during the cycles (Fig. 11f and g).

Furthermore, Que et al. suggested an interesting viewpoint on intentionally bias-induced halide segregation to improve device performance of PeLEDs [91]. An inefficient charge injection issue arising from the different bandgap characteristics of I-rich and Br-rich domains formed by halide segregation is addressed (Fig. 11h). Under an electric field to a PeLED, halide ions start to migrate towards the anode, while halide vacancies move toward the opposite direction (Fig. 11h, left). As a result, I-rich domains are formed near the HTL side due to the different migration speeds of iodide and bromide ions. Since the injected carriers need to face an endergonic process when moving from I-rich to Br-rich domains, the I-rich (narrow-energy-gap) domains near the perovskite/HTL interface dominate radiative recombination. Consequently, there is relatively less radiative recombination in the central region of the perovskite layer and near the perovskite/ETL interface, leading to the inefficient emission characteristics of the PeLED device. In other words, the halide-segregated multiphase formed near the perovskite/HTL interface, despite excellent radiative efficiency in the I-rich domains, limits PeLED devices due to the varying carrier dynamics. On the other hand, strategically placing the halide-segregated multiphase at the grain boundary of the perovskite layer through specific electrical bias, light soaking, or novel approaches is suggested (Fig. 11h, right). The hole injection into wide-bandgap domains can potentially be facilitated by enhanced physical contact between the wide-bandgap domain and HTL. Notably, in addition to hole injection, electron injection should be carefully considered to achieve efficient charge balance with the multiple phases from halide segregation. Although a specific method for implementing this strategy has not been outlined, a new approach to induce such halide segregation may open up intriguing avenues for the enhancement of device performance and stability in PeLEDs.

While numerous strategies have been reported to effectively suppress halide segregation in PeLEDs, these devices still exhibit insufficient stability for real commercialization. PeLEDs must pass stability tests under more stringent conditions, such as 80 °C and 80 % humidity for over 500 h, and this testing must also be met by display panels with R/G/B pixel arrays, not just individual PeLED devices. In other words, without finding effective methods to suppress halide segregation under harsher conditions, the commercialization of PeLEDs will remain challenging. Therefore, it is essential to make significant advancements through research on material design, optimization of materials and doping compositions, manufacturing process improvements, and appropriate encapsulation layers for bright future of PeLEDs.

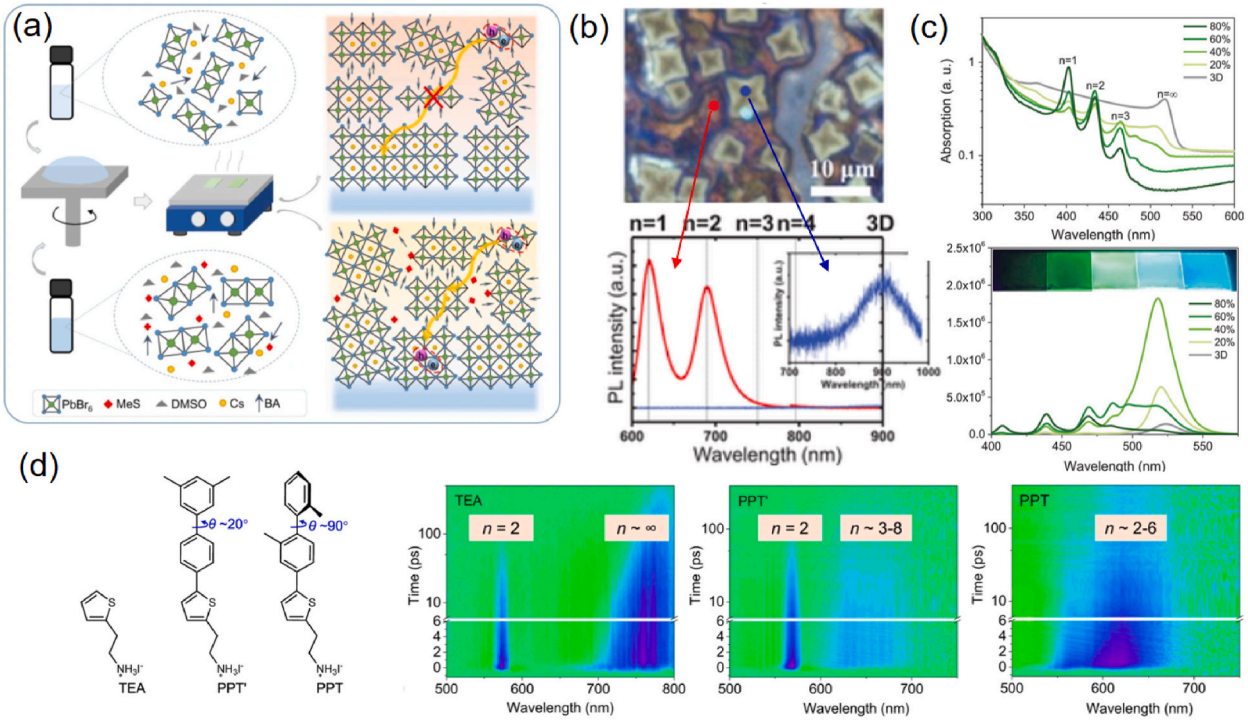

Fig. 12. (a) Schematic diagram of the different energy transfer pathways in the perovskite films prepared by the precursor solutions without and with MeS additive [119]. Copyright 2021 Springer Nature. (b) Optical image and in situ PL spectra of phase-separated $PEA_2MA_2Sn_3I_{10}$ [76]. Copyright 2021 Wiley. (c) UV–vis absorption spectra (top) and PL spectra (bottom) of $CsPbBr_3$ perovskite film with different amounts of PEABr [122]. Copyright 2021 Wiley. (d) Chemical structures of TEA, PPT' and PPT cations (left), and TAS mapping of TEA, PPT' and PPT-based quasi-2D perovskite films (right) [112]. Copyright 2023 Springer Nature.

3. Phase segregation in quasi-2D perovskites

3.1. Dimensionality (n) phase separation

In quasi-2D perovskites, dimensionality (n) has a huge impact on optoelectronic properties for PeLEDs. Small n numbers of $n = 1$ or 2 have significantly low PLQY (generally below 10 % for $n = 1$) due to the strong exciton – phonon interactions [120–122]. When n numbers are near 4, PLQY is high, even reaching above 90 % due to the efficient energy transfer through strong energy funneling [123–126]. On the other hand, n numbers that are too high in quasi-2D perovskites and 3D perovskites have a flat energy landscape, resulting in a lower PLQY [125,127]. As a result, careful control in n numbers for high PLQY can lead to high EQE in PeLED devices with the consideration of the bandgap. However, phase separation disturbs the precise control in n numbers, instead phase-separated quasi-2D perovskite films have undesired n numbers. Therefore, n phase separation in quasi-2D PeLEDs should be suppressed to have high PLQY and controllable emission wavelengths. However, n phase separation in quasi-2D perovskites is thermodynamically favored [128,129]. Formation energy of quasi-2D perovskites decreases when n numbers decrease from $n = 7$ to $n = 1$, indicating $n = 1$ is the most favorable phase in quasi-2D perovskites [128]. Furthermore, enthalpy of formation of quasi-2D perovskites is calculated in addition to the simple calculation of formation energy [129]. Entropy of formation is assumed to be close to zero or slightly decreased, so that the negative enthalpy can result in negative Gibbs free energy of formation. The value of the enthalpy of formation in small n numbers ($n = 1$ to 5) is negative representing a favorable reaction, but that of higher n numbers ($n = 6$ and 7) is positive. Interestingly, the lowest enthalpy of formation occurs when $n = 4$, and it increases sequentially as $n = 2$, 1, 3 and 5 in the favorable reaction. Based on these calculations, crystallization kinetics have been studied to overcome the thermodynamically favored n phase separation.

Yang et al. reported an approach for utilizing methanesulfonate (MeS) additive to control crystallization growth kinetics of quasi-2D perovskites, $(BA)_2Cs_{n-1}Pb_nBr_{3n+1}$ [130]. BA^+ prefers to bind MeS^- rather than Br^- ion due to three hydrogen bonds, which develops higher n numbers because of BA-free nanosheet formation through MeS. In absorption spectra, several excitonic absorption peaks at 403, 434 and 467 nm, corresponding to $n = 1$, 2 and 3, respectively, are highly suppressed in MeS-treated quasi-2D perovskite film. Higher n numbers induced by the MeS additive have efficient energy transfer between different quantum wells (Fig. 12a) [131]. In TAS, ground-state bleach peak corresponding to $n = 2$ in the control film has longer excitation time than that of the MeS-treated film, indicating more excitons are accumulated in $n = 2$ of the control film. Efficient energy transfer to $n > 4$ in the MeS-treated film enables quasi-2D PeLEDs to have high PLQY of 73 % with a high EQE over 20 %, while the control film has only PLQY of 47 % due to the limited energy transfer. As another additive to retard the crystallization rate, chloride was studied for Sn based quasi-2D perovskite films. Without MACl doping, the $(PEA)_2(MA)_2Sn_3I_{10}$ ($n = 3$) quasi-2D perovskite film has non-uniform morphology with cuboid-shaped islands (Fig. 12b, top) [76]. In situ PL spectra representing the cubic morphology shows 3D phase (~900 nm), whereas the background has $n = 1$ and 2 phases (Fig. 12b, bottom). The phase separation into 2D ($n = 1$ and 2) and 3D phases induces low electrical conductivity in lateral direction due to the large energy barrier between 2D and 3D phases [132]. Adding MACl to the quasi-2D perovskite films induces slow crystallization, leading to uniform morphology without the 3D phase. The efficient charge transport via the connected morphology and low energy barriers between small differences in n numbers highly increases electrical conductivity. Contrary to previous studies, fast crystallization via vacuum quenching in 1000 Pa for 90 s between spin-coating and thermal annealing steps was studied to quickly remove excess solvent to accelerate crystallization process of quasi-2D perovskite films [133]. $(PEA)_2Cs_{n-1}Pb_nBr_{3n+1}$ quasi-2D perovskites are formed by mixing PEABr with $CsPbBr_3$ from 0 % to 80 %. Even if the 3D phase is suppressed by the fast crystallization, n phase separation still remains in all quasi-2D perovskite films. When PEABr is added, $n = 1$ and 2 exist in all quasi-2D perovskite films and the 3D phase is removed beyond 40 % of PEABr with the fast crystallization (Fig. 12c). As a result, EL emission wavelength is controlled from green (3D phase) to sky blue (high n numbers) due to energy transfer from small n numbers to high n numbers. Energy transfer in 60 % and 80 % PEABr added quasi-2D perovskite films is inefficient due to the high portion of small n numbers ($n = 1$ and 2), resulting in low EQEs in PeLEDs. Based on the fast crystallization and optimization of PEABr addition, a large scale (3.5×3.5 cm^2) of quasi-2D PeLEDs is demonstrated with over 6 % of EQEs.

In addition to the strategies of the additives and fabrication method, several studies suggested an introduction of bulky organic cations via molecular designs that can efficiently inhibit ionic transport to suppress n phase separation in quasi-2D PeLEDs [123,124]. Thiophenylethylammonium (TEA), (2-(5-(3′,5′-dimethyl-[1,1′-biphenyl]−4-yl)thiophen-2-yl)ethyl-1-ammonium) (PPT') and (2-(5-(2,2′-dimethyl-[1,1′-biphenyl]−4-yl)thiophen-2-yl)ethyl-1-ammonium (PPT) were studied to suppress n phase separation in quasi-2D perovskite films ($n = 3$). The PPT' and PPT have long conjugation lengths adding two phenyl-groups, compared to widely studied TEA (Fig. 12d, left). These PPT' and PPT show 20° and 90° tilted angles between the two phenyl-groups, respectively, which originate from the location of two methyl groups in the last phenyl-group. To compare the ionic transport, 2D perovskite ($n = 1$) films of TEA, PPT', and PPT were exposed to hydrobromic acid vapor. In the TEA_2PbI_4 film, partial substitution of I^- by Br^- induces mixed PL emission from the mixed-halide 2D perovskite film, while PPT' and PPT based 2D perovskite films maintain PL spectra without any shift. Molecular dynamics simulation also supports the same trend that the free energy profiles of vacancy-driven I^- diffusion in the PPT' and PPT based 2D perovskite films are twice higher than that of the TEA based 2D perovskite film. In other words, the ionic transport in 2D perovskites is highly suppressed by PPT' and PPT compared to TEA. Based on the suppressed ionic transport, PPT and PPT' based quasi-2D perovskite films do not have 3D phase, while TEA based quasi-2D perovskite film has dominant 3D phase with $n = 2$. Furthermore, the PPT based quasi-2D perovskite film having uniform n distribution has shorter energy transfer time than the PPT' based qusi-2D perovskite film with the distinct photo bleach peak of $n = 2$ in TAS analysis (Fig. 12d, right). In conclusion, PPT based quasi-2D PeLEDs have high EQEs of over 26 % due to the efficient energy transfer with uniform n distribution.

We have explored the control of crystallization rates for regulating the n-value in quasi-2D perovskites by adding the additives, optimizing the process, and designing the bulky organic cation. Given that efficient energy funneling, driven by uniform n distribution

in quasi-2D perovskites, has been reported to result in high EQEs in PeLEDs, it is anticipated that a wide range of strategies will emerge in future research on the precise control in n numbers in quasi-2D PeLEDs.

3.2. Two-factor phase separation: dimensionality and halide segregation

Even if the thickness of quantum wells has tunability of EL emission wavelengths in PeLEDs, mixing halide ions in quasi-2D perovskites gives more options of EL emission wavelengths. In addition, low dimensionality suppresses halide ion migration that can be expected not to form halide segregation; the free energy barriers for halide diffusion of equatorial direction in pure 2D of $n = 1$ and 3D perovskites are ~12 kcal mol^{-1} and 8.51 kcal mol^{-1}, respectively, estimated by DFT calculation [134]. In the pure 2D perovskite, the free energy barrier of axial direction is higher than the equatorial direction. In other words, halide diffusion in 2D perovskites is highly suppressed in the axial direction, and the equatorial direction is the dominant path for lateral halide diffusion. Based on the halide diffusion pathway, the calculated diffusion coefficient increases when n number is higher and Br ratio in I:Br mixed-halide system increases. Experimentally, Kamat et al. reported lower dimensionality can suppress halide ion migration [135]. Two pure iodide and bromide quasi-2D perovskite films, $(PEA)_2(MA)_{n-1}Pb_nI_{3n+1}$ and $(PEA)_2(MA)_{n-1}Pb_nBr_{3n+1}$ (n = 1, 6, 10), are clamped and heated to monitor the halide diffusion between two separated films. Two distinct excitonic absorption peaks from pure iodide and bromide films are shifted to the middle point after various heating conditions, which results from halide exchange between two films. Based on the rate of the halide exchange, activation energy for the halide diffusion is calculated using Arrhenius relationship. As the dimensionality of quasi-2D perovskite films decreases from $n = 10$ to $n = 6$ and $n = 1$, the activation energy increases from 57.8 kJ/mol to 66.9 kJ/mol and 71.5 kJ/mol. Consequently, halide diffusion can be suppressed by decreasing the dimensionality. Similarly, Janssen et al. investigated halide ion migration of quasi-2D perovskites triggered by light [136]. To examine the halide ion migration induced by the light and halide diffusion under heat, the $(PEA)_2(MA)_3Pb_4(Br_{0.33}I_{0.67})_{13}$ quasi-2D perovskite film is exposed to blue (405 nm) and green (530 nm) light for 3 h, stored in the dark for 14 h and heated at different temperatures for 1 h in sequence. The $(PEA)_2(MA)_3Pb_4(Br_{0.33}I_{0.67})_{13}$ film is phase separated, showing ~2.5 eV for $n = 1$ phase, ~2.3 eV for $n = 2$ phase, and ~1.78 eV for 3D phase in PL spectra (Fig. 13a). Under the light, the PL peak related to the 3D phase is redshifted to ~1.63 eV for 1000 s and the PL peak corresponding to the $n = 2$ phase is also redshifted to ~2.18 eV within 100 s, while there is a negligible shift from the $n = 1$ phase. The redshift of PL emission wavelength originates in iodide-rich domains made by halide ion migration. As a result, the halide ion migration of $n = 1$ phase is more difficult than 3D and $n = 2$ phases under the light. In the dark, the PL peak of the halide-segregated 3D phase is almost recovered to the initial PL emission wavelength by redistributing the halide ions, whereas the PL peak from $n = 2$ phase does not change. When heating the samples at 25 °C, 50 °C, and 70 °C for 1 h, the peak of $n = 2$ phase is gradually recovered as the temperature increases. In other words, the halide diffusion of $n = 2$ phase is highly suppressed compared to 3D phase in dark.

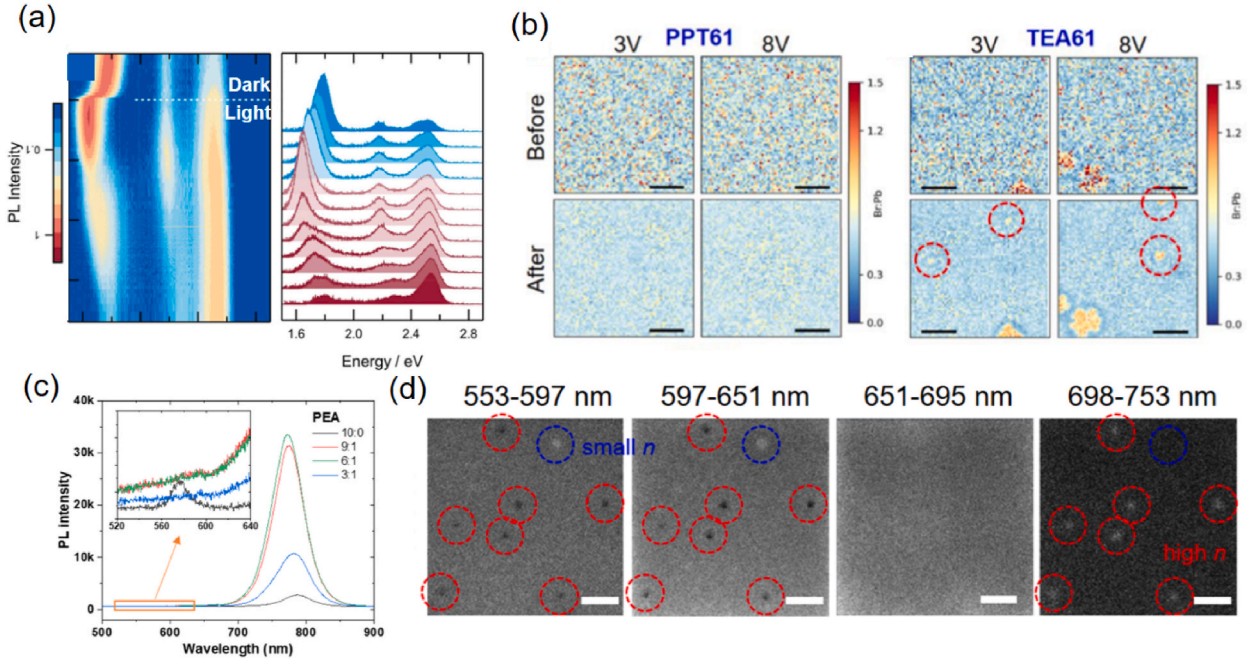

Fig. 13. (a) Normalized 2D mapping of PL intensity (left) and PL spectra versus photon energy (right) of $PEA_2MA_3Pb_4(Br_{0.33}I_{0.67})_{13}$ perovskite film under 10,000 s of continuous excitation (red), and then kept in the dark for 50,000 s (blue) [125]. Copyright 2023 American Chemical Society. (b) In situ XRF mapping for Br:Pb ratio of PPT (left) and TEA (right) based quasi-2D PeLEDs in mixed-halide system (I:Br = 6:1) before and after applying bias of 3 and 8 V. Scale bars are 5 μm. (c) PL spectra of PEA based quasi-2D perovskite films with different I:Br ratio. (d) Confocal PL images of PPP based quasi-2D perovskite film with I:Br = 3:1 [113]. Scale bars: 20 μm. Copyright 2023 American Chemical Society.

In addition to the computational and experimental studies on halide ion migration in quasi-2D perovskites, the analysis of halide diffusion mechanisms is also crucial. Interestingly, the mechanism of the halide diffusion in 2D perovskites does not follow the classic Fickian diffusion model, which is a continuous concentration profile of mixed halide distribution [137]. Two distinct PL peaks of purple and red emission from $(BA)_2PbBr_4$ – $(BA)_2(MA)_2Pb_3I_{10}$ heterostructure create green emission under the heat. The green emission is formed not by continuously being shifted from the purple or red emission, but created as a new peak, and then PL intensity increases without a peak shift. As a result, quantized layer-by-layer diffusion model is proposed depending on a concentration threshold and ion-blocking effects of bulky organic cations. Based on this mechanism, low n numbers can suppress halide ion migration. Moreover, molecular designs for bulky organic cations can significantly decrease the halide diffusion. Dou et al. compared the halide diffusion in 2D perovskites of different types of bulky organic cations using epitaxial heterostructures of $(2T)_2PbI_4$ – $(2T)_2PbBr_4$ and $(BA)_2PbI_4$ – $(BA)_2PbBr_4$, involving bithiophenylethylammonium (2T) and BA [138]. The $(BA)_2PbI_4$ – $(BA)_2PbBr_4$ heterostructure has two distinct peaks of green and purple emission in PL spectra, respectively. After heating at 100 °C for 1 h, the interface of $(BA)_2PbI_4$ – $(BA)_2PbBr_4$ heterostructure becomes ambiguous and PL emission wavelength from $(BA)_2PbI_4$ is blue-shifted due to the halide diffusion. On the other hand, the $(2T)_2PbI_4$ – $(2T)_2PbBr_4$ heterostructure does not have obvious color changes and a peak shift in PL spectra. As a result, the halide diffusion occurs even in pure 2D perovskite ($n = 1$) with BA under the heat, and a molecular design for a bulky organic cation that can suppress the halide diffusion has a significant impact on 2D perovskite research fields.

From a molecular design perspective, well-suppressed halide ion migration in mixed-halide quasi-2D PeLEDs enables tunable emission wavelengths [124]. I:Br ratios of 10:0, 9:1, 6:1 and 3:1 in quasi-2D perovskites ($n = 4$) are investigated for red emission. And PPT, 2-(2″,3′-dimethyl-[1,1′:4′,1″-terphenyl]-4-yl)ethyl-1-ammonium (PPP), TEA, and PEA are compared to study which molecular designs affect two-factor phase separations governed by both n phase separation and halide segregation in mixed-halide quasi-2D perovskite films. PeLED devices of PPT and PPP, which have long conjugation lengths and molecular twist of 90°, have tunable EL

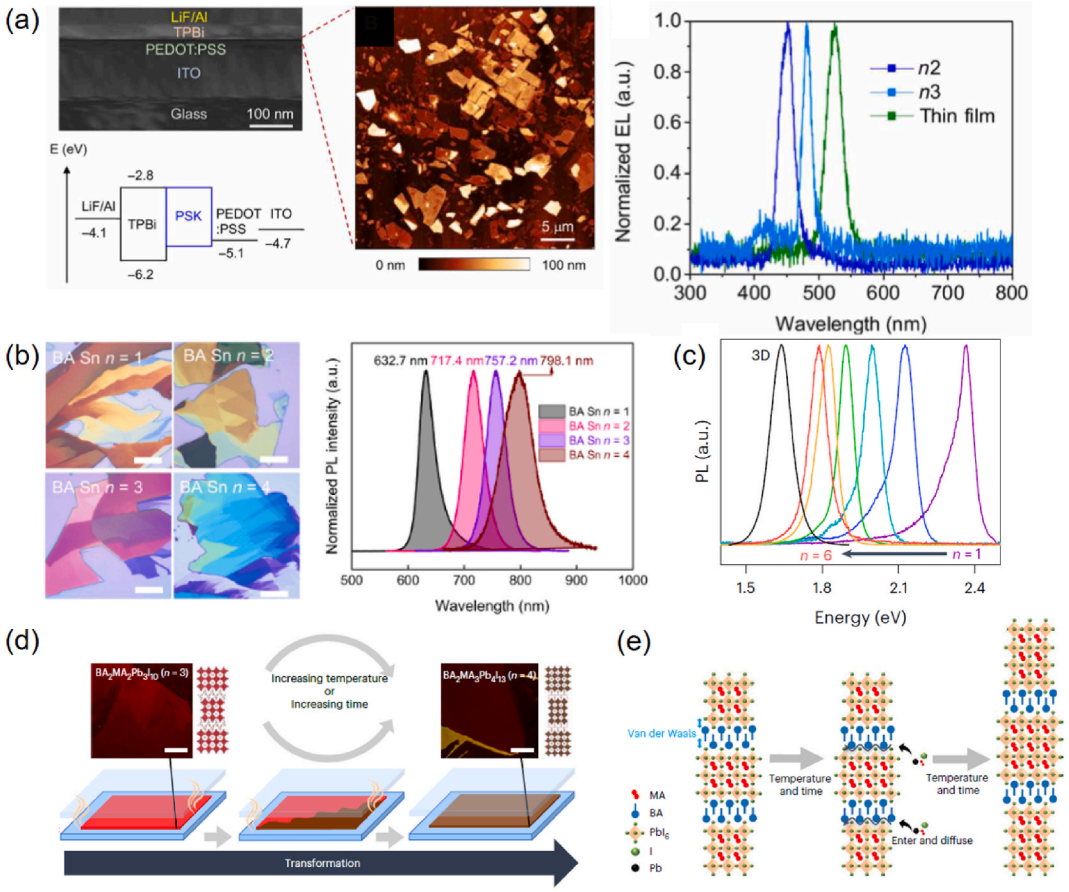

Fig. 14. (a) Cross-sectional SEM image and energy levels of the quasi-2D single crystal perovskite LED device (left). AFM top image of the exfoliated perovskite single crystals of $n2$ (middle). EL spectra of $n2$, $n3$ (single crystal) and thin film based perovskite LEDs (right) [128]. Copyright 2020 American Association for the Advancement of Science. (b) Optical images (left) and PL spectra (right) of phase pure $BA_2MA_{n-1}Sn_nI_{3n+1}$ ($n = 1$ to 4) perovskites synthesized by a mixed-solvent strategy [131]. Copyright 2023 American Association for the Advancement of Science. (c) PL spectra of phase pure quasi-2D perovskite films synthesized by the KCSC method. The schematic illustrations of (d) the KCSC method and (e) the mechanism of formation of high n numbers from the KCSC method [132]. Copyright 2023 Springer Nature.

emission wavelengths from ~680 nm to ~730 nm based on the different I:Br ratios with high EQEs of over 20 %. However, TEA and PEA-based PeLED devices have emission wavelengths near 750 nm regardless of the I:Br ratios, which have low EQEs around 1–2 %, where the emission wavelength corresponds to the 3D phase. Therefore, PPT and PPP can suppress *n* phase separation well compared to TEA and PEA in the mixed-halide system. To compare the halide ion migration of operating devices, the Br:Pb elemental ratio of PPT and TEA based quasi-2D PeLEDs of I:Br = 6:1 (noted as PPT61 and TEA61) was studied using in situ XRF mapping (Fig. 13b). In the TEA61 PeLED device, a Br-rich region showing red color exists even before applying voltages, and new Br-rich regions (depicted by red circles in Fig. 13b) appear when applied to 3V and 8V. This result implies that halide segregation occurs by the electric field in the TEA61 PeLED device. On the other hand, the PPT61 PeLED device has uniform distribution of Br:Pb ratio with and without the bias. In other words, the halide ion migration under the bias is well-suppressed in the quasi-2D PeLED using PPT. In addition, high Br content in I:Br mixed-halide system can accelerate *n* phase separation. In PEA based quasi-2D perovskite films, PL emission from $n = 2$ (~575 nm) disappears and the dominant 3D phase remains when Br content is added (Fig. 13c), which indicates the higher Br contents induce more *n* phase separation. Moreover, even PPP31 film starts forming *n* phase separation, while there is no local *n* phase separation in the other I:Br ratios. In confocal PL mapping, red circles showing longer PL emission wavelength represent higher *n* numbers than the background and blue circles showing shorter PL wavelength indicate smaller *n* numbers (Fig. 13d). This result suggests that while small local phase separation occurs, the presence of a large amount of the Br contents can accelerate the overall *n* phase separation process. Therefore, this strategy of molecular design works well for suppressing the two factor phase separations, but the *n* phase separation in high Br ratios is still challenging in quasi-2D perovskites. Based on the above results, halide segregation can also occur in quasi-2D perovskites. Given the interplay between the *n*-value and mixed halide ratio, careful optimization of both parameters is essential for achieving stable mixed halide quasi-2D PeLEDs.

3.3. Phase-pure quasi-2D perovskite crystals

Although recent studies focusing on the energy funneling effect via uniform *n* distribution have been primarily researched in the field of quasi-2D PeLEDs, efforts to achieve high color purity in PeLEDs using phase-pure quasi-2D perovskites have also been introduced. Yang et al. demonstrated phase-pure quasi-2D PeLEDs using single crystals of $(BA)_2Cs_{n-1}Pb_nBr_{3n+1}$ ($n = 1$, 2 and 3) for blue emission [139]. The single crystals were synthesized by solution temperature lowering, which is heating precursor solutions to make supersaturated solutions followed cooling down. Then, the synthesized crystals are mechanically exfoliated using adhesive tape and transferred to a bottom layer of ITO/PEDOT:PSS (Fig. 14a, left) for the device fabrication. Consequently, EL spectra of the phase-pure quasi-2D PeLED devices of $n = 2$ and 3 single crystals show 450 and 482 nm with a narrow FWHM of 27.5 and 18.1 nm, respectively (Fig. 14a, right). EL spectra of the $n = 1$ based PeLED device is not shown in this study because the emission wavelength of the $n = 1$ single crystal overlaps with the TPBi emission of 410 nm, making it difficult to distinguish between them. For $n = 2$ and 3, the phase-pure quasi-2D PeLEDs using the single crystals are successfully fabricated with the tunable blue EL emission wavelengths. However, perovskite single crystals incorporating PeLED devices still have challenging issues. First, synthesis and transfer method of single crystals have difficulty making uniform thickness. The average thickness of the single crystals is 33.8 nm, but uniformity of the thickness is poor, even having over 100 nm, which may induce non-uniform distribution of EL spectra in the research article of Yang et al. [139]. Second, EQE of 2D PeLEDs is low (around 1 % in the research paper [139]) due to low PLQY and poor charge transport of 2D perovskites. For the low PLQY, the details are explained in section 3.1. Since 2D perovskites prefer to be aligned in-plane direction, bulky organic layers and inorganic octahedron layers are stacked following the *n* numbers in the out-of-plane direction. As a result, charge transport in the out-of-plane direction is restricted as the bulky organic layer acts as an insulating layer. To overcome the poor charge transport, vertical orientation of 2D perovskites using the hot-casting method and solvent engineering [140,141] or high *n* numbers with less bulky organic layers can be a solution. However, single crystals of low *n* numbers or 3D phase can be synthesized easier than those of high *n* numbers [142,143]. Compared to simple elemental competition in the crystal growths of 2D and 3D perovskites, quasi-2D perovskites with high *n* numbers have more complex stacking from different kinds of organic cations, so single-crystal growth of high *n* numbers is more difficult. Therefore, many research groups try to fabricate phase-pure single crystals of high *n* numbers.

Through the analysis of film studies on high *n*-values, we can anticipate the potential future application for phase-pure quasi-2D PeLEDs. Firstly, Shi et al. successfully synthesized single crystals of $(BA)_2(MA)_{n-1}Sn_nI_{3n+1}$ ($n = 1$, 2, 3, and 4) for cavity-free microlasers (Fig. 14b) [135]. In PL spectra, emission wavelengths are 632.7 nm for $n = 1$, 717.4 nm for $n = 2$, 757.2 nm for $n = 3$, and 798.1 nm for $n = 4$, representing phase-pure quasi-2D perovskites (Fig. 14b). Thickness of the $n = 4$ single-crystal is uniform, distributed from 335 to 368 nm. Based on the ultraflat flakes, tunable lasing properties are achieved in the BA-based quasi-2D perovskite single crystals of $n = 2$, 3, and 4. Furthermore, PEA, 2T, 2-([2,2′:5′,2″-terthiophen]-5-yl)ethan-1-aminium (3T) are compared with BA in view of exciton – phonon coupling strength and exciton binding energy. To synthesize the single crystals ($n = 1$ and 2) of PEA, 2T, and 3T, organic solvents are incorporated for moderate polarity. The highest lasing peaks from BA to PEA, 2T, and 3T are shifted because of change in lattice constant, and the lasing threshold decreases due to lowered exciton – phonon coupling strength. Therefore, molecular engineering of bulky organic cations has a significant impact on optoelectronic properties even in the same *n* numbers. In addition, single crystals containing Sn have high chemical stability for preventing Sn oxidation due to grain boundary-less crystal formation. Hence, single crystals can be a future direction for stable optoelectronic devices of Sn-based quasi-2D perovskites. To achieve higher *n* numbers, Mohite et al. reported a new synthesis method, kinetically controlled space confinement (KCSC), for uniform single crystals of $(BA)_2(MA)_{n-1}Pb_nI_{3n+1}$ ($n = 1$ to 6) [143]. The high quality of the single crystals is achieved by the KCSC method, showing continuous peak shifts in PL spectra from $n = 1$ to $n = 6$ (Fig. 14c). The classic synthesis method (solution temperature lowering) induces excessive nucleation due to the fast cooling, resulting in small sizes of single crystals (a few micrometers) [134,137–139]. On the other hand, the

KCSC method prolongs the crystallization kinetics by confining the precursor solution between two glass substrates and heating the solution so that n numbers are gradually increased by elevating temperature and heating time (Fig. 14d). The sandwiched structure by two glass substrates also enables the thickness of the single crystals uniform as ~500 nm. The mechanism for the transformation is that small ions in the precursor solution such as Pb^{2+}, I^{-}, and MA^{+} diffuse into the interfaces between BA layers and inorganic octahedron layers, resulting in high n numbers (Fig. 14e). Based on the mechanism, $n = 3$ single crystal is transformed to $n = 4$, in sequence, and the fully transformed $n = 4$ starts being transformed to $n = 5$, leading to achieving the high purity of n numbers. As the research on the single crystal synthesis of high n numbers in quasi-2D perovskites is growing up, phase-pure quasi-2D PeLEDs can be developed in the foreseeable future such as 3D single crystal-based PeLEDs [144].

4. Conclusion and outlook

In this review, we explored the mechanism of elemental segregation and phase separation in halide perovskites, following various strategies for mitigating these issues. When different elements or dimensionalities are mixed, different stable compositions or crystallization kinetics often lead to heterogeneity in halide perovskite films during the crystallization process. In addition, external stresses such as light, heat, or electric fields can induce ion migration in the completed films or PeLED devices, which drives both elemental segregation and phase separation. Although the general mechanism is similar, the detailed physical origins differ between each element types and quasi-2D perovskites. A-site cations are typically mixed to maintain phase stability, but undesired phases may form in separated regions due to relatively high ion migration rates or early formed elemental segregation during crystallization. B-site cations are less prone to ion migration but Sn perovskites in Pb-Sn alloyed perovskites can induce heterogeneity via Sn oxidation. The X-site ion migration in mixed halide perovskites, commonly used to tune emission wavelengths, occurs most readily, often reducing color purity, selectivity, and stability of PeLEDs. In quasi-2D perovskites, 2D/3D phase separation occurs due to the low formation energy of $n = 1$ perovskites and the strong interactions between bulky organic cations. Furthermore, we introduce the concept of two-factor phase separations (n phase separation and halide segregation) in mixed-halide quasi-2D perovskites. The interplay between controlling the n numbers and mixing halide ions reveals a significant correlation, necessitating the simultaneous consideration of dimensionality and mixed-halide ratios in mixed-halide quasi-2D PeLEDs.

To gain deeper insights into these mechanisms and their impact on device performance, it is crucial to utilize appropriate analytical techniques. Here, we briefly summarize the key methods for investigating elemental segregation and phase separation, as well as analyzing the optoelectronic properties influenced by these phenomena. Techniques such as IR, XRF, EDX spectroscopy, as well as ToF-SIMS analysis, are commonly used to compare the elemental distribution within perovskite films, while structural analyses, including GIXRD and PL spectroscopy, are widely employed for both 3D and quasi-2D perovskites. For quasi-2D perovskites, tracking changes in the bleaching peaks observed in TAS effectively shows energy transfer between different n numbers, which is critical for understanding energy funneling process.

Compositional engineering in halide perovskites is a key strategy for achieving high efficiency and stability in PeLEDs, enabling both phase stability and tunable emission wavelengths. However, when elements are mixed, elemental segregation can occur, eliminating the benefits. Therefore, careful optimization of the composition is essential. Quasi-2D perovskites, despite facing challenges with 2D/3D phase separation, have demonstrated high EQEs of over 25 % in PeLEDs through efficient energy funneling. Additionally, phase-pure perovskites hold promise for PeLEDs with high color purity and low defect density. However, their operational stability remains lower than that of 3D PeLEDs. With better suppression of ion migration and their inherent hydrophobicity, and environmental stability, quasi-2D perovskites present significant potential for future advancements through various strategic approaches.

CRediT authorship contribution statement

Seok Joo Yang: Writing – review & editing, Writing – original draft, Investigation, Formal analysis, Data curation, Conceptualization. **Yoon Ho Lee:** Writing – review & editing, Writing – original draft. **Kagachi Tateno:** Writing – review & editing, Writing – original draft. **Letian Dou:** Writing – review & editing, Supervision, Conceptualization.

Declaration of competing interest

The authors declare the following financial interests/personal relationships which may be considered as potential competing interests: Letian Dou, Purdue University.

Acknowledgments

This work is supported by the National Science Foundation (Grant No. 2131608-ECCS and 2143568-DMR).

Appendix A. Supplementary data

Supplementary data to this article can be found online at https://doi.org/10.1016/j.pquantelec.2024.100537.

References

[1] L. Protesescu, S. Yakunin, M.I. Bodnarchuk, F. Krieg, R. Caputo, C.H. Hendon, R.X. Yang, A. Walsh, M.V. Kovalenko, Nanocrystals of cesium lead halide perovskites ($CsPbX_3$, X = Cl, Br, and I): novel optoelectronic materials showing bright emission with wide color gamut, Nano Lett. 15 (2015) 3692–3696, https://doi.org/10.1021/nl5048779.

[2] Y.-H. Kim, S. Kim, A. Kakekhani, J. Park, J. Park, Y.-H. Lee, H. Xu, S. Nagane, R.B. Wexler, D.-H. Kim, S.H. Jo, L. Martínez-Sarti, P. Tan, A. Sadhanala, G.-S. Park, Y.-W. Kim, B. Hu, H.J. Bolink, S. Yoo, R.H. Friend, A.M. Rappe, T.-W. Lee, Comprehensive defect suppression in perovskite nanocrystals for high-efficiency light-emitting diodes, Nat. Photonics 15 (2021) 148–155, https://doi.org/10.1038/s41566-020-00732-4.

[3] Y.-H. Kim, H. Cho, T.-W. Lee, Metal halide perovskite light emitters, Proc. Natl. Acad. Sci. U. S. A 113 (2016) 11694–11702, https://doi.org/10.1073/pnas.1607471113.

[4] T.-H. Han, K.Y. Jang, Y. Dong, R.H. Friend, E.H. Sargent, T.-W. Lee, A roadmap for the commercialization of perovskite light emitters, Nat. Rev. Mater. 7 (2022) 757–777, https://doi.org/10.1038/s41578-022-00459-4.

[5] J.S. Kim, J.-M. Heo, G.-S. Park, S.-J. Woo, C. Cho, H.J. Yun, D.-H. Kim, J. Park, S.-C. Lee, S.-H. Park, E. Yoon, N.C. Greenham, T.-W. Lee, Ultra-bright, efficient and stable perovskite light-emitting diodes, Nature 611 (2022) 688–694, https://doi.org/10.1038/s41586-022-05304-w.

[6] W. Bai, T. Xuan, H. Zhao, H. Dong, X. Cheng, L. Wang, R.-J. Xie, Perovskite light-emitting diodes with an external quantum efficiency exceeding 30, Adv. Mater. 35 (2023) e2302283, https://doi.org/10.1002/adma.202302283.

[7] S. Tao, I. Schmidt, G. Brocks, J. Jiang, I. Tranca, K. Meerholz, S. Olthof, Absolute energy level positions in tin- and lead-based halide perovskites, Nat. Commun. 10 (2019) 2560, https://doi.org/10.1038/s41467-019-10468-7.

[8] G.E. Eperon, S.D. Stranks, C. Menelaou, M.B. Johnston, L.M. Herz, H.J. Snaith, Formamidinium lead trihalide: a broadly tunable perovskite for efficient planar heterojunction solar cells, Energy Environ. Sci. 7 (2014) 982–988, https://doi.org/10.1039/C3EE43822H.

[9] B. Zhao, M. Abdi-Jalebi, M. Tabachnyk, H. Glass, V.S. Kamboj, W. Nie, A.J. Pearson, Y. Puttisong, K.C. Godel, H.E. Beere, D.A. Ritchie, A.D. Mohite, S. E. Dutton, R.H. Friend, A. Sadhanala, High open-circuit voltages in tin-rich low-bandgap perovskite-based planar heterojunction photovoltaics, Adv. Mater. 29 (2017) 1604744, https://doi.org/10.1002/adma.201604744.

[10] Z. Li, M. Yang, J.-S. Park, S.-H. Wei, J.J. Berry, K. Zhu, Stabilizing perovskite structures by tuning tolerance factor: formation of formamidinium and cesium lead iodide solid-state alloys, Chem. Mater. 28 (2015) 284–292, https://doi.org/10.1021/acs.chemmater.5b04107.

[11] J.-W. Xiao, L. Liu, D. Zhang, N. De Marco, J.-W. Lee, O. Lin, Q. Chen, Y. Yang, The emergence of the mixed perovskites and their applications as solar cells, Adv. Energy Mater. 7 (2017) 1700491, https://doi.org/10.1002/aenm.201700491.

[12] Z. Wang, Z. Shi, T. Li, Y. Chen, W. Huang, Stability of perovskite solar cells: a prospective on the substitution of the A cation and X anion, Angew. Chem. Int. Ed. 56 (2017) 1190–1212, https://doi.org/10.1002/anie.201603694.

[13] V.M. Goldschmidt, Die Gesetze der Krystallochemie, Naturwissensaften 14 (1926) 477–485, https://doi.org/10.1007/BF01507527.

[14] J.-W. Lee, D.-H. Kim, H.-S. Kim, S.-W. Seo, S.M. Cho, N.-G. Park, Formamidinium and cesium hybridization for photo- and moisture-stable perovskite solar cell, Adv. Energy Mater. 5 (2015) 1501310, https://doi.org/10.1002/aenm.201501310.

[15] Y.H. Park, I. Jeong, S. Bae, H.J. Son, P. Lee, J. Lee, C.-H. Lee, M.J. Ko, Inorganic rubidium cation as an enhancer for photovoltaic performance and moisture stability of $HC(NH_2)_2PbI_3$ perovskite solar cells, Adv. Funct. Mater. 27 (2017) 1605988, https://doi.org/10.1002/adfm.201605988.

[16] T. Duong, H.K. Mulmudi, H. Shen, Y. Wu, C. Barugkin, Y.O. Mayon, H.T. Nguyen, D. Macdonald, J. Peng, M. Lockrey, W. Li, Y.-B. Cheng, T.P. White, K. Weber, K. Catchpole, Structural engineering using rubidium iodide as a dopant under excess lead iodide conditions for high efficiency and stable perovskites, Nano Energy 30 (2016) 330–340, https://doi.org/10.1016/j.nanoen.2016.10.027.

[17] E. Bi, Z. Song, C. Li, Z. Wu, Y. Yan, Mitigating ion migration in perovskite solar cells, Trends Chem 3 (2021) 575–588, https://doi.org/10.1016/j.trechm.2021.04.004.

[18] P.V. Kamat, M. Kuno, Halide ion migration in perovskite nanocrystals and nanostructures, Acc. Chem. Res. 54 (2021) 520–531, https://doi.org/10.1021/acs.accounts.0c00749.

[19] J.T. DuBose, P.V. Kamat, Hole trapping in halide perovskites induces phase segregation, Acc. Mater. Res. 3 (2022) 761–771, https://doi.org/10.1021/accountsmr.2c00076.

[20] W. Fu, A.G. Ricciardulli, Q.A. Akkerman, R.A. John, M.M. Tavakoli, S. Essig, M.V. Kovalenko, M. Saliba, Stability of perovskite materials and devices, Mater. Today 58 (2022) 275–296, https://doi.org/10.1016/j.mattod.2022.06.020.

[21] C. Eames, J.M. Frost, P.R. Barnes, B.C. O'Regan, A. Walsh, M.S. Islam, Ionic transport in hybrid lead iodide perovskite solar cells, Nat. Commun. 6 (2015) 7497, https://doi.org/10.1038/ncomms8497.

[22] J.M. Azpiroz, E. Mosconi, J. Bisquert, F. De Angelis, Defect migration in methylammonium lead iodide and its role in perovskite solar cell operation, Energy Environ. Sci. 8 (2015) 2118–2127, https://doi.org/10.1039/C5EE01265A.

[23] Y. Yuan, J. Huang, Ion migration in organometal trihalide perovskite and its impact on photovoltaic efficiency and stability, Acc. Chem. Res. 49 (2016) 286–293, https://doi.org/10.1021/acs.accounts.5b00420.

[24] L. Etgar, The merit of perovskite's dimensionality; can this replace the 3D halide perovskite? Energy Environ. Sci. 11 (2018) 234–242, https://doi.org/10.1039/C7EE03397D.

[25] D. Marongiu, M. Saba, F. Quochi, A. Mura, G. Bongiovanni, The role of excitons in 3D and 2D lead halide perovskites, J. Mater. Chem. C 7 (2019) 12006–12018, https://doi.org/10.1039/C9TC04292J.

[26] T. Ishihara, X. Hong, J. Ding, A.V. Nurmikko, Dielectric confinement effect for exciton and biexciton states in PbI4-based two-dimensional semiconductor structures, Surf. Sci. 267 (1992) 323–326, https://doi.org/10.1016/0039-6028(92)91147-4.

[27] L. Mao, C.C. Stoumpos, M.G. Kanatzidis, Two-dimensional hybrid halide perovskites: principles and promises, J. Am. Chem. Soc. 141 (2019) 1171–1190, https://doi.org/10.1021/jacs.8b10851.

[28] M. Saliba, T. Matsui, J.-Y. Seo, K. Domanski, J.P. Correa-Baena, M.K. Nazeeruddin, S.M. Zakeeruddin, W. Tress, A. Abate, A. Hagfeldt, M. Gratzel, Cesium-containing triple cation perovskite solar cells: improved stability, reproducibility and high efficiency, Energy Environ. Sci. 9 (2016) 1989–1997, https://doi.org/10.1039/C5EE03874J.

[29] T.J. Jacobsson, S. Svanström, V. Andrei, J.P.H. Rivett, N. Kornienko, B. Philippe, U.B. Cappel, H. Rensmo, F. Deschler, G. Boschloo, Extending the compositional space of mixed lead halide perovskites by Cs, Rb, K, and Na doping, J. Phys. Chem. C 122 (2018) 13548–13557, https://doi.org/10.1021/acs.jpcc.7b12464.

[30] B. Cao, L. Yang, S. Jiang, H. Lin, N. Wang, X. Li, Flexible quintuple cation perovskite solar cells with high efficiency, J. Mater. Chem. A 7 (2019) 4960–4970, https://doi.org/10.1039/C8TA11945G.

[31] C. Li, A. Wang, L. Xie, X. Deng, K. Liao, J.-a. Yang, T. Li, F. Hao, Emerging alkali metal ion (Li^+, Na^+, K^+ and Rb^+) doped perovskite films for efficient solar cells: recent advances and prospects, J. Mater. Chem. A 7 (2019) 24150–24163, https://doi.org/10.1039/C9TA08130E.

[32] K. Wang, W.S. Subhani, Y. Wang, X. Zuo, H. Wang, L. Duan, S.F. Liu, Metal cations in efficient perovskite solar cells: progress and perspective, Adv. Mater. 31 (2019) e1902037, https://doi.org/10.1002/adma.201902037.

[33] J.-W. Lee, D.-J. Seol, A.-N. Cho, N.-G. Park, High-efficiency perovskite solar cells based on the black polymorph of $HC(NH_2)_2PbI_3$, Adv. Mater. 26 (2014) 4991–4998, https://doi.org/10.1002/adma.201401137.

[34] A. Binek, F.C. Hanusch, P. Docampo, T. Bein, Stabilization of the trigonal high-temperature phase of formamidinium lead iodide, J. Phys. Chem. Lett. 6 (2015) 1249–1253, https://doi.org/10.1021/acs.jpclett.5b00380.

[35] N. Pellet, P. Gao, G. Gregori, T.-Y. Yang, M.K. Nazeeruddin, J. Maier, M. Gratzel, Mixed-organic-cation perovskite photovoltaics for enhanced solar-light harvesting, Angew. Chem. Int. Ed. 53 (2014) 3151–3157, https://doi.org/10.1002/anie.201309361.

[36] D.J. Kubicki, D. Prochowicz, A. Hofstetter, S.M. Zakeeruddin, M. Gratzel, L. Emsley, Phase segregation in Cs-, Rb- and K-doped mixed-cation $(MA)_x(FA)_{1-x}PbI_3$ hybrid perovskites from solid-state NMR, J. Am. Chem. Soc. 139 (2017) 14173–14180, https://doi.org/10.1021/jacs.7b07223.

[37] Z. Liang, Y. Zhang, H. Xu, W. Chen, B. Liu, J. Zhang, H. Zhang, Z. Wang, D.-H. Kang, J. Zeng, X. Gao, Q. Wang, H. Hu, H. Zhou, X. Cai, X. Tian, P. Reiss, B. Xu, T. Kirchartz, Z. Xiao, S. Dai, N.-G. Park, J. Ye, X. Pan, Homogenizing out-of-plane cation composition in perovskite solar cells, Nature 624 (2023) 557–563, https://doi.org/10.1038/s41586-023-06784-0.

[38] L. Chen, Y.-Y. Tan, Z.-X. Chen, T. Wang, S. Hu, Z.A. Nan, L.-Q. Xie, Y. Hui, J.-X. Huang, C. Zhan, S.-H. Wang, J.-Z. Zhou, J.-W. Yan, B.-W. Mao, Z.-Q. Tian, Toward long-term stability: single-crystal alloys of cesium-containing mixed cation and mixed halide perovskite, J. Am. Chem. Soc. 141 (2019) 1665–1671, https://doi.org/10.1021/jacs.8b11610.

[39] H.-S. Kim, N.-G. Park, Importance of tailoring lattice strain in halide perovskite crystals, NPG Asia Mater. 12 (2020) 78, https://doi.org/10.1038/s41427-020-00265-w.

[40] R. Chatterjee, I.M. Pavlovetc, K. Aleshire, G.V. Hartland, M. Kuno, Subdiffraction infrared imaging of mixed cation perovskites: probing local cation heterogeneities, ACS Energy Lett. 3 (2018) 469–475, https://doi.org/10.1021/acsenergylett.7b01306.

[41] E. Smith, G. Dent, Modern Raman Spectroscopy: A Practical Approach, WILEY, West Sussex, 2005.

[42] Y. Lin, B. Chen, Y. Fang, J. Zhao, C. Bao, Z. Yu, Y. Deng, P.N. Rudd, Y. Yan, Y. Yuan, J. Huang, Excess charge-carrier induced instability of hybrid perovskites, Nat. Commun. 9 (2018) 4981, https://doi.org/10.1038/s41467-018-07438-w.

[43] C. Bischoff, K. Schuller, S.P. Beckman, S.W. Martin, Non-Arrhenius ionic conductivities in glasses due to a distribution of activation energies, Phys. Rev. Lett. 109 (2012) 075901, https://doi.org/10.1103/PhysRevLett.109.075901.

[44] J.B. Goodenough, Electronic and ionic transport properties and other physical aspects of perovskites, Rep. Prog. Phys. 67 (2004) 1915–1993, https://doi.org/10.1088/0034-4885/67/11/R01.

[45] J. Xing, Q. Wang, Q. Dong, Y. Yuan, Y. Fang, J. Huang, Ultrafast ion migration in hybrid perovskite polycrystalline thin films under light and suppression in single crystals, Phys. Chem. Chem. Phys. 18 (2016) 30484–30490, https://doi.org/10.1039/C6CP06496E.

[46] K. Domanski, B. Roose, T. Matsui, M. Saliba, S.-H. Turren-Cruz, J.-P. Correa-Baena, C.R. Carmona, G. Richardson, J.M. Foster, F. De Angelis, J.M. Ball, A. Petrozza, N. Mine, M.K. Nazeeruddin, W. Tress, M. Grätzel, U. Steiner, A. Hagfeldt, A. Abate, Migration of cations induces reversible performance losses over day/night cycling in perovskite solar cells, Energy Environ. Sci. 10 (2017) 604–613, https://doi.org/10.1039/C6EE03352K.

[47] A. Walsh, D.O. Scanlon, S. Chen, X.G. Gong, S.-H. Wei, Self-regulation mechanism for charged point defects in hybrid halide perovskites, Angew. Chem. Int. Ed. 54 (2015) 1791–1794, https://doi.org/10.1002/anie.201409740.

[48] J.A. Christians, P. Schulz, J.S. Tinkham, T.H. Schloemer, S.P. Harvey, B.J. Tremolet de Villers, A. Sellinger, J.J. Berry, J.M. Luther, Tailored interfaces of unencapsulated perovskite solar cells for >1,000 hour operational stability, Nat. Energy 3 (2018) 68–74, https://doi.org/10.1038/s41560-017-0067-y.

[49] N. Li, Y. Luo, Z. Chen, X. Niu, X. Zhang, J. Lu, R. Kumar, J. Jiang, H. Liu, X. Guo, B. Lai, G. Brocks, Q. Chen, S. Tao, D.P. Fenning, H. Zhou, Microscopic degradation in formamidinium-cesium lead iodide perovskite solar cells under operational stressors, Joule 4 (2020) 1743–1758, https://doi.org/10.1016/j.joule.2020.06.005.

[50] J. Tong, Z. Song, D.H. Kim, X. Chen, C. Chen, A.F. Palmstrom, P.F. Ndione, M.O. Reese, S.P. Dunfield, G. Reid Obadiah, J. Liu, F. Zhang, S.P. Harvey, Z. Li, S. T. Christensen, G. Teeter, D. Zhao, M.M. Al-Jassim, M.F.A.M.v. Hest, M.C. Beard, S.E. Shaheen, J.J. Berry, Y. Yan, K. Zhu, Carrier lifetimes of >1 μs in Sn-Pb perovskites enable efficient all-perovskite tandem solar cells, Science 364 (2019) 475–479, https://doi.org/10.1126/science.aav7911.

[51] D. Zhao, C. Chen, C. Wang, M.M. Junda, Z. Song, C.R. Grice, Y. Yu, C. Li, B. Subedi, N.J. Podraza, X. Zhao, G. Fang, R.-G. Xiong, K. Zhu, Y. Yan, Efficient two-terminal all-perovskite tandem solar cells enabled by high-quality low-bandgap absorber layers, Nat. Energy 3 (2018) 1093–1100, https://doi.org/10.1038/s41560-018-0278-x.

[52] R. Lin, K. Xiao, Z. Qin, Q. Han, C. Zhang, M. Wei, M.I. Saidaminov, Y. Gao, J. Xu, M. Xiao, A. Li, J. Zhu, E.H. Sargent, H. Tan, Monolithic all-perovskite tandem solar cells with 24.8% efficiency exploiting comproportionation to suppress Sn(II) oxidation in precursor ink, Nat. Energy 4 (2019) 864–873, https://doi.org/10.1038/s41560-019-0466-3.

[53] K. Xiao, R. Lin, Q. Han, Y. Hou, Z. Qin, H.T. Nguyen, J. Wen, M. Wei, V. Yeddu, M.I. Saidaminov, Y. Gao, X. Luo, Y. Wang, H. Gao, C. Zhang, J. Xu, J. Zhu, E. H. Sargent, H. Tan, All-perovskite tandem solar cells with 24.2% certified efficiency and area over 1 cm^2 using surface-anchoring zwitterionic antioxidant, Nat. Energy 5 (2020) 870–880, https://doi.org/10.1038/s41560-020-00705-5.

[54] J. Tong, Q. Jiang, A.J. Ferguson, A.F. Palmstrom, X. Wang, J. Hao, S.P. Dunfield, A.E. Louks, S.P. Harvey, C. Li, H. Lu, R.M. France, S.A. Johnson, F. Zhang, M. Yang, J.F. Geisz, M.D. McGehee, M.C. Beard, Y. Yan, D. Kuciauskas, J.J. Berry, K. Zhu, Carrier control in Sn–Pb perovskites via 2D cation engineering for all-perovskite tandem solar cells with improved efficiency and stability, Nat. Energy 7 (2022) 642–651, https://doi.org/10.1038/s41560-022-01046-1.

[55] F. Hao, C.C. Stoumpos, R.P. Chang, M.G. Kanatzidis, Anomalous band gap behavior in mixed Sn and Pb perovskites enables broadening of absorption spectrum in solar cells, J. Am. Chem. Soc. 136 (2014) 8094–8099, https://doi.org/10.1021/ja5033259.

[56] J. Im, C.C. Stoumpos, H. Jin, A.J. Freeman, M.G. Kanatzidis, Antagonism between spin-orbit coupling and steric effects causes anomalous band gap evolution in the perovskite photovoltaic materials $CH_3NH_3Sn_{1-x}Pb_xI_3$, J. Phys. Chem. Lett. 6 (2015) 3503–3509, https://doi.org/10.1021/acs.jpclett.5b01738.

[57] A. Goyal, S. McKechnie, D. Pashov, W. Tumas, M. van Schilfgaarde, V. Stevanović, Origin of pronounced nonlinear band gap behavior in lead–tin hybrid perovskite alloys, Chem. Mater. 30 (2018) 3920–3928, https://doi.org/10.1021/acs.chemmater.8b01695.

[58] H. Lee, S.B. Kang, S. Lee, K. Zhu, D.H. Kim, Progress and outlook of Sn-Pb mixed perovskite solar cells, Nano Converg 10 (2023) 27, https://doi.org/10.1186/s40580-023-00371-9.

[59] D. Ricciarelli, D. Meggiolaro, F. Ambrosio, F. De Angelis, Instability of tin iodide perovskites: bulk p-doping versus surface tin oxidation, ACS Energy Lett. 5 (2020) 2787–2795, https://doi.org/10.1021/acsenergylett.0c01174.

[60] W. Liao, D. Zhao, Y. Yu, C.R. Grice, C. Wang, A.J. Cimaroli, P. Schulz, W. Meng, K. Zhu, R.-G. Xiong, Y. Yan, Lead-free inverted planar formamidinium tin triiodide perovskite solar cells achieving power conversion efficiencies up to 6.22, Adv. Mater. 28 (2016) 9333–9340, https://doi.org/10.1002/adma.201602992.

[61] M.H. Kumar, S. Dharani, W.L. Leong, P.P. Boix, R.R. Prabhakar, T. Baikie, C. Shi, H. Ding, R. Ramesh, M. Asta, M. Graetzel, S.G. Mhaisalkar, N. Mathews, Lead-free halide perovskite solar cells with high photocurrents realized through vacancy modulation, Adv. Mater. 26 (2014) 7122–7127, https://doi.org/10.1002/adma.201401991.

[62] S.J. Lee, S.S. Shin, Y.C. Kim, D. Kim, T.K. Ahn, J.H. Noh, J. Seo, S.I. Seok, Fabrication of efficient formamidinium tin iodide perovskite solar cells through SnF_2-pyrazine complex, J. Am. Chem. Soc. 138 (2016) 3974–3977, https://doi.org/10.1021/jacs.6b00142.

[63] Q. Tai, X. Guo, G. Tang, P. You, T.-W. Ng, D. Shen, J. Cao, C.-K. Liu, N. Wang, Y. Zhu, C.-S. Lee, F. Yan, Antioxidant grain passivation for air-stable tin-based perovskite solar cells, Angew. Chem. Int. Ed. 58 (2019) 806–810, https://doi.org/10.1002/anie.201811539.

[64] H. Min, N. Wang, N. Chen, Y. Tong, Y. Wang, J. Wang, J. Liu, S. Wang, X. Wu, P. Yang, H. Shi, C. Zhuo, Q. Chen, J. Li, D. Zhang, X. Lu, C. Zhu, Q. Peng, L. Zhu, J. Chang, W. Huang, J. Wang, Spin coating epitaxial heterodimensional tin perovskites for light-emitting diodes, Nat. Nanotechnol. (2024), https://doi.org/10.1038/s41565-023-01588-9.

[65] H. Min, J. Chang, Y. Tong, J. Wang, F. Zhang, Z. Feng, X. Bi, N. Chen, Z. Kuang, S. Wang, L. Yuan, H. Shi, N. Zhao, D. Qian, S. Xu, L. Zhu, N. Wang, W. Huang, J. Wang, Additive treatment yields high-performance lead-free perovskite light-emitting diodes, Nat. Photonics 17 (2023) 755–760, https://doi.org/10.1038/s41566-023-01231-y.

[66] F. Yuan, G. Folpini, T. Liu, U. Singh, A. Treglia, J.W.M. Lim, J. Klarbring, S.I. Simak, I.A. Abrikosov, T.C. Sum, A. Petrozza, F. Gao, Bright and stable near-infrared lead-free perovskite light-emitting diodes, Nat. Photonics 18 (2024) 170–176, https://doi.org/10.1038/s41566-023-01351-5.

[67] X. Jiang, H. Li, Q. Zhou, Q. Wei, M. Wei, L. Jiang, Z. Wang, Z. Peng, F. Wang, Z. Zang, K. Xu, Y. Hou, S. Teale, W. Zhou, R. Si, X. Gao, E.H. Sargent, Z. Ning, One-step synthesis of SnI_2·$(DMSO)_x$ adducts for high-performance tin perovskite solar cells, J. Am. Chem. Soc. 143 (2021) 10970–10976, https://doi.org/10.1021/jacs.1c03032.

[68] F. Gu, S. Ye, Z. Zhao, H. Rao, Z. Liu, Z. Bian, C. Huang, Improving performance of lead-free formamidinium tin triiodide perovskite solar cells by tin source purification, Sol. RRL 2 (2018) 1800136, https://doi.org/10.1002/solr.201800136.

[69] Z. Qin, M. Pols, M. Qin, J. Zhang, H. Yan, S. Tao, X. Lu, Over-18%-Efficiency quasi-2D ruddlesden-popper Pb-Sn mixed perovskite solar cells by compositional engineering, ACS Energy Lett. 8 (2023) 3188–3195, https://doi.org/10.1021/acsenergylett.3c00853.

[70] K. Liang, D.B. Mitzi, M.T. Prikas, Synthesis and Characterization of organic-inorganic perovskite thin films prepared using a versatile two-step dipping technique, Chem. Mater. 10 (1998) 403–411, https://doi.org/10.1021/cm970568f.

[71] T. Yokoyama, D.H. Cao, C.C. Stoumpos, T.B. Song, Y. Sato, S. Aramaki, M.G. Kanatzidis, Overcoming short-circuit in lead-free $CH_3NH_3SnI_3$ perovskite solar cells via kinetically controlled gas-solid reaction film fabrication process, J. Phys. Chem. Lett. 7 (2016) 776–782, https://doi.org/10.1021/acs.jpclett.6b00118.

[72] S.D. Stranks, G.E. Eperon, G. Grancini, C. Menelaou, M.J. Alcocer, T. Leijtens, L.M. Herz, A. Petrozza, H.J. Snaith, Electron-hole diffusion lengths exceeding 1 micrometer in an organometal trihalide perovskite absorber, Science 342 (2013) 341–344, https://doi.org/10.1126/science.1243982.

[73] E.L. Unger, A.R. Bowring, C.J. Tassone, V.L. Pool, A. Gold-Parker, R. Cheacharoen, K.H. Stone, E.T. Hoke, M.F. Toney, M.D. McGehee, Chloride in lead chloride-derived organo-metal halides for perovskite-absorber solar cells, Chem. Mater. 26 (2014) 7158–7165, https://doi.org/10.1021/cm503828b.

[74] J. Kim, T. Hwang, S. Lee, B. Lee, J. Kim, G.S. Jang, S. Nam, B. Park, Solvent and intermediate phase as boosters for the perovskite transformation and solar cell performance, Sci. Rep. 6 (2016) 25648, https://doi.org/10.1038/srep25648.

[75] S.J. Yang, M. Kim, H. Ko, D.H. Sin, J.H. Sung, J. Mun, J. Rho, M.-H. Jo, K. Cho, Visualization and investigation of charge transport in mixed-halide perovskite via lateral-structured photovoltaic devices, Adv. Funct. Mater. 28 (2018) 1804067, https://doi.org/10.1002/adfm.201804067.

[76] S.J. Yang, D. Kim, J. Choi, S.H. Kim, K. Park, S. Ryu, K. Cho, Enhancing thermoelectric power factor of 2D organometal halide perovskites by suppressing 2D/3D phase separation, Adv. Mater. 33 (2021) e2102797, https://doi.org/10.1002/adma.202102797.

[77] S.J. Yang, J. Choi, S. Song, C. Park, K. Cho, Enhancing air-stability and reproducibility of lead-free formamidinium-based tin perovskite solar cell by chlorine doping, Sol. Energy Mater. Sol. Cells 227 (2021) 111072, https://doi.org/10.1016/j.solmat.2021.111072.

[78] J. Choi, S.J. Yang, S.G. Han, W. Sung, D. Yoo, K. Cho, Defect-stabilized tin-based perovskite solar cells enabled by multifunctional molecular additives, Chem. Mater. 35 (2023) 1148–1158, https://doi.org/10.1021/acs.chemmater.2c03141.

[79] M. Hu, C. Bi, Y. Yuan, Y. Bai, J. Huang, Stabilized wide bandgap $MAPbBr_xI_{3-x}$ perovskite by enhanced grain size and improved crystallinity, Adv. Sci. 3 (2016) 1500301, https://doi.org/10.1002/advs.201500301.

[80] Z. Chen, G. Brocks, S. Tao, P.A. Bobbert, Unified theory for light-induced halide segregation in mixed halide perovskites, Nat. Commun. 12 (2021) 2687, https://doi.org/10.1038/s41467-021-23008-z.

[81] M. Karlsson, Z. Yi, S. Reichert, X. Luo, W. Lin, Z. Zhang, C. Bao, R. Zhang, S. Bai, G. Zheng, P. Teng, L. Duan, Y. Lu, K. Zheng, T. Pullerits, C. Deibel, W. Xu, R. Friend, F. Gao, Mixed halide perovskites for spectrally stable and high-efficiency blue light-emitting diodes, Nat. Commun. 12 (2021) 361, https://doi.org/10.1038/s41467-020-20582-6.

[82] S. Draguta, O. Sharia, S.J. Yoon, M.C. Brennan, Y.V. Morozov, J.S. Manser, P.V. Kamat, W.F. Schneider, M. Kuno, Rationalizing the light-induced phase separation of mixed halide organic-inorganic perovskites, Nat. Commun. 8 (2017) 200, https://doi.org/10.1038/s41467-017-00284-2.

[83] Z. Xiao, L. Zhao, N.L. Tran, Y.L. Lin, S.H. Silver, R.A. Kerner, N. Yao, A. Kahn, G.D. Scholes, B.P. Rand, Mixed-halide perovskites with stabilized bandgaps, Nano Lett. 17 (2017) 6863–6869, https://doi.org/10.1021/acs.nanolett.7b03179.

[84] Z. Yang, A. Rajagopal, S.B. Jo, C.-C. Chueh, S. Williams, C.-C. Huang, J.K. Katahara, H.W. Hillhouse, A.K.-Y. Jen, Stabilized wide bandgap perovskite solar cells by tin substitution, Nano Lett. 16 (2016) 7739–7747, https://doi.org/10.1021/acs.nanolett.6b03857.

[85] E.M. Hutter, L.A. Muscarella, F. Wittmann, J. Versluis, L. McGovern, H.J. Bakker, Y.-W. Woo, Y.-K. Jung, A. Walsh, B. Ehrler, Thermodynamic stabilization of mixed-halide perovskites against phase segregation, Cell Rep. Phys. Sci. 1 (2020) 100120, https://doi.org/10.1016/j.xcrp.2020.100120.

[86] J. Xu, C.C. Boyd, Z.J. Yu, A.F. Palmstrom, D.J. Witter, B.W. Larson, R.M. France, J. Werner, S.P. Harvey, E.J. Wolf, W. Weigand, S. Manzoor, M.F.A.M. van Hest, J.J. Berry, J.M. Luther, Z.C. Holman, M.D. McGehee, Triple-halide wide-band gap perovskites with suppressed phase segregation for efficient tandems, Science 367 (2020) 1097–1104, https://doi.org/10.1126/science.aaz507.

[87] I.L. Braly, R.J. Stoddard, A. Rajagopal, A.R. Uhl, J.K. Katahara, A.K.-Y. Jen, H.W. Hillhouse, Current-induced phase segregation in mixed halide hybrid perovskites and its impact on two-terminal tandem solar cell design, ACS Energy Lett. 2 (2017) 1841–1847, https://doi.org/10.1021/acsenergylett.7b00525.

[88] W. Rehman, D.P. McMeekin, J.B. Patel, R.L. Milot, M.B. Johnston, H.J. Snaith, L.M. Herz, Photovoltaic mixed-cation lead mixed-halide perovskites: links between crystallinity, photo-stability and electronic properties, Energy Environ. Sci. 10 (2017) 361–369, https://doi.org/10.1039/C6EE03014A.

[89] H.X. Dang, K. Wang, M. Ghasemi, M.-C. Tang, M. De Bastiani, E. Aydin, E. Dauzon, D. Barrit, J. Peng, D.-M. Smilgies, S. De Wolf, A. Amassian, Multi-cation synergy suppresses phase segregation in mixed-halide perovskites, Joule 3 (2019) 1746–1764, https://doi.org/10.1016/j.joule.2019.05.016.

[90] D.P. McMeekin, G. Sadoughi, W. Rehman, G.E. Eperon, M. Saliba, M.T. Horantner, A. Haghighirad, N. Sakai, L. Korte, B. Rech, M.B. Johnson, L.M. Herz, H. J. Snaith, A mixed-cation lead mixed-halide perovskite absorber for tandem solar cells, Science 351 (2016) 151–155, https://doi.org/10.1126/science.aad5845.

[91] Y. Guo, X. Yin, D. Liu, W. Que, Photo/current-induced halide segregation in mixed-halide perovskites-based devices, Trends Chem 5 (2023) 509–511, https://doi.org/10.1016/j.trechm.2023.04.007.

[92] A.F. Gualdrón-Reyes, S.J. Yoon, E.M. Barea, S. Agouram, V. Muñoz-Sanjosé, Á.M. Meléndez, M.E. Niño-Gómez, I. Mora-Seró, Controlling the phase segregation in mixed halide perovskites through nanocrystal size, ACS Energy Lett. 4 (2019) 54–62, https://doi.org/10.1021/acsenergylett.8b02207.

[93] A.D. Wright, J.B. Patel, M.B. Johnston, L.M. Herz, Temperature-dependent reversal of phase segregation in mixed-halide perovskites, Adv. Mater. 35 (2023) e2210834, https://doi.org/10.1002/adma.202210834.

[94] T. Elmelund, B. Seger, M. Kuno, P.V. Kamat, How interplay between photo and thermal activation dictates halide ion segregation in mixed halide perovskites, ACS Energy Lett. 5 (2019) 56–63, https://doi.org/10.1021/acsenergylett.9b02265.

[95] D. Pan, Y. Fu, J. Chen, K.J. Czech, J.C. Wright, S. Jin, Visualization and studies of ion-diffusion kinetics in cesium lead bromide perovskite nanowires, Nano Lett. 18 (2018) 1807–1813, https://doi.org/10.1021/acs.nanolett.7b05023.

[96] M. Lai, A. Obliger, D. Lu, C.S. Kley, C.G. Bischak, Q. Kong, T. Lei, L. Dou, N.S. Ginsberg, D.T. Limmer, P. Yang, Intrinsic anion diffusivity in lead halide perovskites is facilitated by a soft lattice, Proc. Natl. Acad. Sci. U. S. A 115 (2018) 11929–11934, https://doi.org/10.1073/pnas.1812718115.

[97] Z. Xiao, Y. Yuan, Y. Shao, Q. Wang, Q. Dong, C. Bi, P. Sharma, A. Gruverman, J. Huang, Giant switchable photovoltaic effect in organometal trihalide perovskite devices, Nat. Mater. 14 (2015) 193–198, https://doi.org/10.1038/nmat4150.

[98] D. Di Girolamo, N. Phung, F.U. Kosasih, F. Di Giacomo, F. Matteocci, J.A. Smith, M.A. Flatken, H. Köbler, S.H. Turren Cruz, A. Mattoni, L. Cinà, B. Rech, A. Latini, G. Divitini, C. Ducati, A. Di Carlo, D. Dini, A. Abate, Ion migration-induced amorphization and phase segregation as a degradation mechanism in planar perovskite solar cells, Adv. Energy Mater. 10 (2020) 2000310, https://doi.org/10.1002/aenm.202000310.

[99] Y. Yuan, T. Li, Q. Wang, J. Xing, A. Gruverman, J. Huang, Anomalous photovoltaic effect in organic-inorganic hybrid perovskite solar cells, Sci. Adv. 3 (2017) e1602164, https://doi.org/10.1126/sciadv.1602164.

[100] M.C. Brennan, S. Draguta, P.V. Kamat, M. Kuno, Light-induced anion phase segregation in mixed halide perovskites, ACS Energy Lett. 3 (2017) 204–213, https://doi.org/10.1021/acsenergylett.7b01151.

[101] P. Mathew, J. Cho, P.V. Kamat, Ramifications of ion migration in 2D lead halide perovskites, ACS Energy Lett. 9 (2024) 1103–1114, https://doi.org/10.1021/acsenergylett.4c00093.

[102] D. Di Girolamo, F. Matteocci, F.U. Kosasih, G. Chistiakova, W. Zuo, G. Divitini, L. Korte, C. Ducati, A. Di Carlo, D. Dini, A. Abate, Stability and dark hysteresis correlate in NiO-based perovskite solar cells, Adv. Energy Mater. 9 (2019) 1901642, https://doi.org/10.1002/aenm.201901642.

[103] M. Noman, Z. Khan, S.T. Jan, A comprehensive review on the advancements and challenges in perovskite solar cell technology, RSC Adv. 14 (2024) 5085–5131, https://doi.org/10.1039/D3RA07518D.

[104] S. Liu, V.P. Biju, Y. Qi, W. Chen, Z. Liu, Recent progress in the development of high-efficiency inverted perovskite solar cells, NPG Asia Mater. 15 (2023) 27, https://doi.org/10.1038/s41427-023-00474-z.

[105] A.J. Knight, L.M. Herz, Preventing phase segregation in mixed-halide perovskites: a perspective, Energy Environ. Sci. 13 (2020) 2024–2046, https://doi.org/10.1039/D0EE00788A.

[106] F. Peña-Camargo, P. Caprioglio, F. Zu, E. Gutierrez-Partida, C.M. Wolff, K. Brinkmann, S. Albrecht, T. Riedl, N. Koch, D. Neher, M. Stolterfoht, Halide segregation versus interfacial recombination in bromide-rich wide-gap perovskite solar cells, ACS Energy Lett. 5 (2020) 2728–2736, https://doi.org/10.1021/acsenergylett.0c01104.

[107] K.A. Bush, K. Frohna, R. Prasanna, R.E. Beal, T. Leijtens, S.A. Swifter, M.D. McGehee, Compositional engineering for efficient wide band gap perovskites with improved stability to photoinduced phase segregation, ACS Energy Lett. 3 (2018) 428–435, https://doi.org/10.1021/acsenergylett.7b01255.
[108] R.J. Stoddard, A. Rajagopal, R.L. Palmer, I.L. Braly, A.K.-Y. Jen, H.W. Hillhouse, Enhancing defect tolerance and phase stability of high-bandgap perovskites via guanidinium alloying, ACS Energy Lett. 3 (2018) 1261–1268, https://doi.org/10.1021/acsenergylett.8b00576.
[109] R.A. Belisle, K.A. Bush, L. Bertoluzzi, A. Gold-Parker, M.F. Toney, M.D. McGehee, Impact of surfaces on photoinduced halide segregation in mixed-halide perovskites, ACS Energy Lett. 3 (2018) 2694–2700, https://doi.org/10.1021/acsenergylett.8b01562.
[110] M. Abdi-Jalebi, Z. Andaji-Garmaroudi, S. Cacovich, C. Stavrakas, B. Philippe, J.M. Richter, M. Alsari, E.P. Booker, E.M. Hutter, A.J. Pearson, S. Lilliu, T. J. Savenije, H. Rensmo, G. Divitini, C. Ducati, R.H. Friend, S.D. Stranks, Maximizing and stabilizing luminescence from halide perovskites with potassium passivation, Nature 555 (2018) 497–501, https://doi.org/10.1038/nature25989.
[111] J. Wen, Y. Zhao, P. Wu, Y. Liu, X. Zheng, R. Lin, S. Wan, K. Li, H. Luo, Y. Tian, L. Li, H. Tan, Heterojunction formed via 3D-to-2D perovskite conversion for photostable wide-bandgap perovskite solar cells, Nat. Commun. 14 (2023) 7118, https://doi.org/10.1038/s41467-023-43016-5.
[112] S. Zhang, H. Liu, X. Li, S. Wang, Enhancing quantum yield of $CsPb(Br_xCl_{1-x})_3$ nanocrystals through lanthanum doping for efficient blue light-emitting diodes, Nano Energy 77 (2020) 105302, https://doi.org/10.1016/j.nanoen.2020.105302.
[113] F. Zhang, X. Zhang, C. Wang, M. Sun, X. Luo, Y. Yang, S. Chang, D. Zhang, L. Duan, Nano Energy 79 (2021) 105486, https://doi.org/10.1016/j.nanoen.2020.105486.
[114] F. Zhang, J. Song, B. Cai, X. Chen, C. Wei, T. Fang, H. Zeng, Stabilizing electroluminescence color of blue perovskite LEDs via amine group doping, Sci. Bull. 66 (2021) 2189–2198, https://doi.org/10.1016/j.scib.2021.04.033.
[115] L. Zhang, Y. Jiang, Y. Feng, M. Cui, S. Li, X. Fu, H.-Y. Hsu, C. Qin, M. Yuan, Manipulating local lattice distortion for spectrally stable and efficient mixed-halide blue perovskite LEDs, Angew. Chem. 62 (2023) e202302184, https://doi.org/10.1002/anie.202302184.
[116] T. Chiba, J. Sato, S. Ishikawa, Y. Takahashi, H. Ebe, S. Sumikoshi, S. Ohisa, J. Kido, Neodymium chloride-doped perovskite nanocrystals for efficient blue light-emitting devices, ACS Appl. Mater. Interfaces 12 (2020) 53891–53898, https://doi.org/10.1021/acsami.0c11736.
[117] L. Cheng, C. Yi, Y. Tong, L. Zhu, G. Kusch, X. Wang, X. Wang, T. Jiang, H. Zhang, J. Zhang, C. Xue, H. Chen, W. Xu, D. Liu, R.A. Oliver, R.H. Friend, L. Zhang, N. Wang, W. Huang, J. Wang, Halide Homogenization for High-Performance Blue Perovskite Electroluminescence, Research 2020, 2020 9017871, https://doi.org/10.34133/2020/9017871.
[118] Y. Ke, N. Wang, D. Kong, Y. Cao, Y. He, L. Zhu, Y. Wang, C. Xue, Q. Peng, F. Gao, W. Huang, J. Wang, Defect passivation for red perovskite light-emitting diodes with improved brightness and stability, J. Phys. Chem. Lett. 10 (2019) 380–385, https://doi.org/10.1021/acs.jpclett.8b03664.
[119] C.G. Bischak, C.L. Hetherington, H. Wu, S. Aloni, D.F. Ogletree, D.T. Limmer, N.S. Ginsberg, Origin of reversible photoinduced phase separation in hybrid perovskites, Nano Lett. 17 (2017) 1028–1033, https://doi.org/10.1021/acs.nanolett.6b04453.
[120] Z. Wang, F. Wang, B. Zhao, S. Qu, T. Hayat, A. Alsaedi, L. Sui, K. Yuan, J. Zhang, Z. Wei, Z. Tan, Efficient two-dimensional tin halide perovskite light-emitting diodes via a spacer cation substitution strategy, J. Phys. Chem. Lett. 11 (2020) 1120–1127, https://doi.org/10.1021/acs.jpclett.9b03565.
[121] T. Zhang, C. Zhou, X. Feng, N. Dong, H. Chen, X. Chen, L. Zhang, J. Lin, J. Wang, Regulation of the luminescence mechanism of two-dimensional tin halide perovskites, Nat. Commun. 13 (2022) 60, https://doi.org/10.1038/s41467-021-27663-0.
[122] Y.-H. Chang, J.-C. Lin, Y.-C. Chen, T.-R. Kuo, D.-Y. Wang, Facile synthesis of two-dimensional Ruddlesden-Popper perovskite quantum dots with fine-tunable optical properties, Nanoscale Res. Lett. 13 (2018) 247, https://doi.org/10.1186/s11671-018-2664-5.
[123] K. Wang, Z.-Y. Lin, Z. Zhang, L. Jin, K. Ma, A.H. Coffey, H.R. Atapattu, Y. Gao, J.Y. Park, Z. Wei, B.P. Finkenauer, C. Zhu, X. Meng, S.N. Chowdhury, Z. Chen, T. Terlier, T.-H. Do, Y. Yao, K.R. Graham, A. Boltasseva, T.-F. Guo, L. Huang, H. Gao, B.M. Savoie, L. Dou, Suppressing phase disproportionation in quasi-2D perovskite light-emitting diodes, Nat. Commun. 14 (2023) 397, https://doi.org/10.1038/s41467-023-36118-7.
[124] S.J. Yang, K. Wang, Y. Luo, J.Y. Park, H. Yang, A.H. Coffey, K. Ma, J. Sun, S. Wieghold, C. Zhu, L. Dou, Two-factor phase separations in mixed-halide quasi-2D perovskite LEDs: dimensionality and halide segregations, ACS Energy Lett. 8 (2023) 3693–3701, https://doi.org/10.1021/acsenergylett.3c01009.
[125] Y. Jiang, M. Cui, S. Li, C. Sun, Y. Huang, J. Wei, L. Zhang, M. Lv, C. Qin, Y. Liu, M. Yuan, Reducing the impact of Auger recombination in quasi-2D perovskite light-emitting diodes, Nat. Commun. 12 (2021) 336, https://doi.org/10.1038/s41467-020-20555-9.
[126] Y. Jiang, J. Wei, M. Yuan, Energy-funneling process in quasi-2D perovskite light-emitting diodes, J. Phys. Chem. Lett. 12 (2021) 2593–2606, https://doi.org/10.1021/acs.jpclett.1c00072.
[127] L.N. Quan, Y. Zhao, F.P. Garcia de Arquer, R. Sabatini, G. Walters, O. Voznyy, R. Comin, Y. Li, J.Z. Fan, H. Tan, J. Pan, M. Yuan, O.M. Bakr, Z. Lu, D.H. Kim, E. H. Sargent, Tailoring the energy landscape in quasi-2D halide perovskites enables efficient green-light emission, Nano Lett. 17 (2017) 3701–3709, https://doi.org/10.1021/acs.nanolett.7b00976.
[128] J. Xing, Y. Zhao, M. Askerka, L.N. Quan, X. Gong, W. Zhao, J. Zhao, H. Tan, G. Long, L. Gao, Z. Yang, O. Voznyy, J. Tang, Z.-H. Lu, Q. Xiong, E.H. Sargent, Color-stable highly luminescent sky-blue perovskite light-emitting diodes, Nat. Commun. 9 (2018) 3541, https://doi.org/10.1038/s41467-018-05909-8.
[129] C.M.M. Soe, G.P. Nagabhushana, R. Shivaramaiah, H. Tsai, W. Nie, J.-C. Blancon, F. Melkonyan, D.H. Cao, B. Traoré, L. Pedesseau, M. Kepenekian, C. Katan, J. Even, T.J. Marks, A. Navrotsky, A.D. Mohite, C.C. Stoumpos, M.G. Kanatzidis, Structural and thermodynamic limits of layer thickness in 2D halide perovskites, Proc. Natl. Acad. Sci. U. S. A 116 (2019) 58–66, https://doi.org/10.1073/pnas.1811006115.
[130] L. Kong, X. Zhang, Y. Li, H. Wang, Y. Jiang, S. Wang, M. You, C. Zhang, T. Zhang, S.V. Kershaw, W. Zheng, Y. Yang, Q. Lin, M. Yuan, A.L. Rogach, X. Yang, Smoothing the energy transfer pathway in quasi-2D perovskite films using methanesulfonate leads to highly efficient light-emitting devices, Nat. Commun. 12 (2021) 1246, https://doi.org/10.1038/s41467-021-21522-8.
[131] L. Lei, D. Seyitliyev, S. Stuard, J. Mendes, Q. Dong, X. Fu, Y.-A. Chen, S. He, X. Yi, L. Zhu, C.-H. Chang, H. Ade, K. Gundogdu, F. So, Efficient energy funneling in quasi-2D perovskites: from light emission to lasing, Adv. Mater. 32 (2020) e1906571, https://doi.org/10.1002/adma.201906571.
[132] Z. Wang, Q. Lin, F.P. Chmiel, N. Sakai, L.M. Herz, H.J. Snaith, Efficient ambient-air-stable solar cells with 2D–3D heterostructured butylammonium-caesium-formamidinium lead halide perovskites, Nat. Energy 2 (2017) 17135, https://doi.org/10.1038/nenergy.2017.135.
[133] C. Chen, L. Zeng, Z. Jiang, Z. Xu, Y. Chen, Z. Wang, S. Chen, B. Xu, Y. Mai, F. Guo, Vacuum-assisted preparation of high-quality quasi-2D perovskite thin films for large-area light-emitting diodes, Adv. Funct. Mater. 32 (2021) 2107644, https://doi.org/10.1002/adfm.202107644.
[134] S. Zhang Akriti, Z.-Y. Lin, E. Shi, B.P. Finkenauer, Y. Gao, A.J. Pistone, K. Ma, B.M. Savoie, L. Dou, Quantifying anionic diffusion in 2D halide perovskite lateral heterostructures, Adv. Mater. 33 (2021) 2105183, https://doi.org/10.1002/adma.202105183.
[135] J. Cho, J.T. DuBose, A.N.T. Le, P.V. Kamat, Suppressed halide ion migration in 2D lead halide perovskites, ACS Mater. Lett. 2 (2020) 565–570, https://doi.org/10.1021/acsmaterialslett.0c00124.
[136] K. Datta, A. Caiazzo, M.A. Hope, J. Li, A. Mishra, M. Cordova, Z. Chen, L. Emsley, M.M. Wienk, R.A.J. Janssen, Light-induced halide segregation in 2D and quasi-2D mixed-halide perovskites, ACS Energy Lett. 8 (2023) 1662–1670, https://doi.org/10.1021/acsenergylett.3c00160.
[137] E. Shi Akriti, S.B. Shiring, J. Yang, C.L. Atencio-Martinez, B. Yuan, X. Hu, Y. Gao, B.P. Finkenauer, A.J. Pistone, Y. Yu, P. Liao, B.M. Savoie, L. Dou, Layer-by-layer anionic diffusion in two-dimensional halide perovskite vertical heterostructures, Nat. Nanotechnol. 16 (2021) 584–591, https://doi.org/10.1038/s41565-021-00848-w.
[138] E. Shi, B. Yuan, S.B. Shiring, Y. Gao, Akriti, Y. Guo, C. Su, M. Lai, P. Yang, J. Kong, B.M. Savoie, Y. Yu, L. Dou, Two-dimensional halide perovskite lateral epitaxial heterostructures, Nature 580 (2020) 614–620, https://doi.org/10.1038/s41586-020-2219-7.
[139] H. Chen, J. Lin, J. Kang, Q. Kong, D. Lu, J. Kang, M. Lai, L.N. Quan, Z. Lin, J. Jin, L.-W. Wang, M.F. Toney, P. Yang, Structural and spectral dynamics of single-crystalline Ruddlesden-Popper phase halide perovskite blue light-emitting diodes, Sci. Adv. 6 (2020) eaay4045, https://doi.org/10.1126/sciadv.aay4045.
[140] H. Tsai, W. Nie, J.-C. Blancon, C.C. Stoumpos, R. Asadpour, B. Harutyunyan, A.J. Neukirch, R. Verduzco, J.J. Crochet, S. Tretiak, L. Pedesseau, J. Even, M. A. Alam, G. Gupta, J. Lou, P.M. Ajayan, M.J. Bedzyk, M.G. Kanatzidis, High-efficiency two-dimensional Ruddlesden-Popper perovskite solar cells, Nature 536 (2016) 312–316, https://doi.org/10.1038/nature18306.
[141] A.H. Coffey, S.J. Yang, M. Gómez, B.P. Finkenauer, T. Terlier, C. Zhu, L. Dou, Controlling crystallization of quasi-2D perovskite solar cells: incorporating bulky conjugated ligands, Adv. Energy Mater. 13 (2022) 2201501, https://doi.org/10.1002/aenm.202201501.

[142] Y. Li, H. Zhou, M. Xia, H. Shen, T. Wang, H. Gao, X. Sheng, Y. Han, Z. Chen, L. Dou, H. Zhu, E. Shi, Phase-pure 2D tin halide perovskite thin flakes for stable lasing, Sci. Adv. 9 (2023) eadh0517, https://doi.org/10.1126/sciadv.adh0517.
[143] J. Hou, W. Li, H. Zhang, S. Sidhik, J. Fletcher, I. Metcalf, S.B. Anantharaman, X. Shuai, A. Mishra, J.-C. Blancon, C. Katan, D. Jariwala, J. Even, M.G. Kanatzidis, A.D. Mohite, Synthesis of 2D perovskite crystals via progressive transformation of quantum well thickness, Nat. Synth. 3 (2023) 265–275, https://doi.org/10.1038/s44160-023-00422-3.
[144] W. Chen, Z. Huang, H. Yao, Y. Liu, Y. Zhang, Z. Li, H. Zhou, P. Xiao, T. Chen, H. Sun, J. Huang, Z. Xiao, Highly bright and stable single-crystal perovskite light-emitting diodes, Nat. Photonics 17 (2023) 401–407, https://doi.org/10.1038/s41566-023-01167-3.